1 2 9 0

UNIVERSIDADE D
COIMBRA

Ivo Arcanjo Jorge Bene Sengo

NEUTRON STAR CRUST
Effects of Rotation and Strong Magnetic Fields

Dissertação no âmbito do mestrado em Física, ramo de Física Nuclear e de Partículas, orientada pela Professora Doutora Constança Providência e pela Doutora Helena Pais, e apresentada ao Departamento de Física da Faculdade de Ciências e Tecnologia da Universidade de Coimbra.

Outubro de 2019

Faculty of Sciences and Technology
University of Coimbra

Neutron Star Crust: Effects of Rotation and Strong Magnetic Fields

Ivo Arcanjo Jorge Bene Sengo

VOLUME 1

A thesis written in fulfilment of the requirements for the Physics MSc Program, supervised by Prof. Dr. Constança Providência and Dr. Helena Pais.

October 2019

UNIVERSIDADE D
COIMBRA

Resumo

Estrelas de neutrões constituem uma área de estudo fascinante, não apenas pelas inúmeras incógnitas em torno da sua composição interna, mas também por protagonizarem alguns dos fenómenos astrofísicos mais misteriosos que se observa. Fenómenos extremos tais como mudanças bruscas no frequência de rotação, *glitches*, e as erupções expontâneas de enormes quantidades de energia, *flares*, acreditam-se estar associados à região da crosta das estrelas de neutrões. Estrelas de neutrões possuem campos magnéticos intensos e podem exibir frequências de rotação extremamente altas. Estes dois atributos fazem com que certas considerações de simetria, deixem de ser válidas, o que exige um tratamento que tenha em consideração todas as particularidades da relatividade geral. Neste trabalho pretende-se estudar os efeitos da rotação e de campos magnéticos intensos nas propriedades da crosta de estrelas de neutrões. Para isso recorremos à biblioteca, em código aberto, de relatividade numérica LORENE.

É sabido que, devido aos efeitos de campos magnéticos intensos, a transição da região da crosta para o núcleo é marcada por uma zona intermédia onde coexiste matéria estável e instável, à que nós chamamos de *crosta alargada*. Neste trabalho pretendemos perceber de que forma esta região se relaciona com as propriedades globais da estrela, e de que forma depende dos parâmetros da equação de estado. Em particular, pretendemos averiguar se a crosta, incluindo a região alargada, contém a zona onde a força de Lorenz muda de sinal. Para além disso, pretendemos verificar se o máximo da força de Lorenz ocorre na região da crosta. Acreditamos que ao responder à estas perguntas, poder-se-ão elucidar alguns aspetos relativos aos fenómenos extremos típicos da crosta.

Abstract

Neutron stars provide an exciting field of study, not only for the many open questions regarding their internal composition, but also for some of the most puzzling astrophysical phenomena, not observed in other types of stars. Extreme phenomena such as rapid changes in the rotational frequency, *glitches*, and the sudden release of huge amounts of energy, *flares*, are believed to be associated with the crust region of neutron stars. Neutrons stars are highly magnetized objects and can also show very high rotation frequencies. Those two features restrict some of the symmetry considerations that we could take advantage of, and claim for a fully general relativistic treatment. In this thesis we study the effects of strong magnetic fields and of rotation on the properties of neutron stars' crust under a fully general relativistic framework. In order to achieve that, we make use of the open source numerical relativity library LORENE.

It is understood that, due to the effects of strong magnetic fields, the transition from the crust region to the core is characterized by an intermediate region where stable and unstable matter interchange, that we here call the *extended crust*. In this work we try to understand how this region relates to the global properties of the star, and how does it depend on the parameters of the equation of state. In particular we ascertain whether the crust, equipped with its extended region, contains the region where the Lorenz force changes sign. In addition to that, we ask whether the Lorenz force takes a maximum inside the crust region. We believe that by answering those questions we might shed some light onto the extreme phenomena associated with the crust region of neutron stars.

Agradecimentos

Gostaria, em primeiro lugar, de agradecer à Prof.ª Doutora Constança Providência e à Doutora Helena Pais por me terem introduzido ao tema e pelo acompanhamento que me deram, sempre marcado por muita paciência e disponibilidade.

Não podia deixar de agradecer aos professores Fernando Nogueira, José António Paixão, Rui Ferreira Marques e, novamente, Constança Providência pela atenção que tiveram perante aos problemas a que estive sujeito aquando da minha entrada para o mestrado.

Agradeço também aos meus colegas e amigos que fazem com que a distância de casa seja menos avassaladora. Nisto não podia deixar de agradecer à minha amiga Mª Inês, por estar sempre atenta à minha saúde emocional.

Por fim, gostaria de agradecer aos meus pais e à minha irmã, cujo apoio é um ótimo exemplo de *não-localidade* .

Contents

List of Figures

List of Tables

Chapter 1

Introduction

> *[...] the density of matter becomes so great that atomic nuclei come in close contact, forming one giant nucleus.*
>
> Lev Landau

1.1 Neutron Stars

Neutrons stars are the remnants of the collapse of a giant star: from a star with more than eight solar masses and a radius bigger than 10^8 km, emerges a smaller star of 10 km, with a mass comparable to that of our Sun. Matter inside these stars reach the highest values of density permitted in Nature – neutron stars are 10^{14} times denser than Earth.

In addition to their extreme densities, neutron stars also posses strong magnetic fields, ranging from 10^8 – 10^{15} G and can rotate at frequencies up to at least 700 Hz [3, 4].

The structure of neutron stars can be subdivided into five regions: the atmosphere, the outer crust, the inner crust, the outer core and the inner core (cf. Figure 1.1).

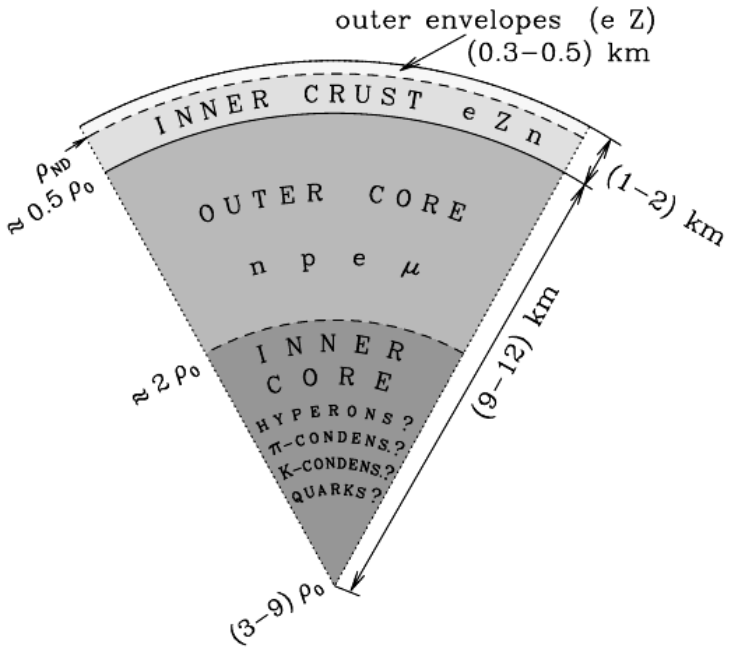

Figure 1.1: Structure of a neutron star. Figure taken from [1].

The **atmosphere** is a thin layer of plasma that varies from some ten centimetres to a few millimetres. The **outer crust** extends for some hundred meters, starting from the atmosphere bottom layer to the region where the density, ρ, is is equal to the density at which free neutrons drip from nuclei (*neutron drip* density) : $\rho = \rho_{ND} \approx 4 \cdot 10^{11}$ g cm^{-3}. The **inner crust** occupies most of the crust region, with a thickness of about one kilometre. It starts from ρ_{ND} to about one half of the saturation density of nuclear matter, ρ_0, the density of nucleon matter in heavy atomic nuclei. In the inner crust, just below nuclear saturation density, nuclear matter may be found in a variety of geometrical shapes, other than the spherical one [5]. These different phases of matter are called *pasta phases* and include gnocchi-like semi-spherical geometries, spaghetti-like rods, and lasagna-like slabs – hence the name *pasta*.

The **outer core** comprehends densities from approximately $0.5\rho_0$ to $\sim 2\rho_0$. This region is populated by neutrons, protons , electrons and possibly muons . The electrons and muons form almost ideal Fermi gases, whilst neutrons and protons form a strongly

interacting Fermi liquid, that might as well be in a superfluid state. The inner core starts from around $2\rho_0$. There is no yet a consensus regarding its internal composition. The many hypothesis include the presence of hyperons, pion condensates, kaon condensates and even quark matter [1].

1.2 Outline

In this thesis we focus on the effects of strong magnetic fields and rotation on the properties of the crust. We start, in Chapter 2, by presenting the model that we use to describe the neutron star matter. We also discuss the formalism from which we obtained the range of densities that correspond to the crust-core transition, when strong magnetic fields are involved.

The calculation of rotating highly magnetized stars demands a fully general relativistic treatment. In Chapter 3 we introduce the basic concepts of numerical relativity. In Chapter 4 we present a numerical relativity framework for calculations of rotating and/or magnetized stars.

Finally, in Chapter 5 we present the results of our work. These results were obtained through a set of numerical simulations performed with the open access library LORENE [6].

Chapter 2

Neutron Star Matter

The astrophysical properties of the star, such as radius and mass, are obtained by solving Einstein's equations. Our solution will depend on the model that we use to describe the matter inside the star, i.e., the particles that we suspect to exist there and their interactions. Such information is contained in the form of a thermodynamical equation relating state variables of the system – the equation of state (EOS). In the case of neutron star matter, such equation is normally written in the form $p(\epsilon)$ or $\epsilon(p)$, where p is the pressure and ϵ is the energy density. Supplied with an EOS, one can then construct the energy-momentum tensor that acts as source for the gravitational field. When spheric symmetry is applicable (when we ignore both rotation and magnetic fields), we can use our EOS to obtain the mass and radius of the star by solving the, much simpler, Tolman–Oppenheimer–Volkoff (TOV) system of equations:

$$\begin{cases} \frac{\mathrm{d}p}{\mathrm{d}r} & = -\frac{(\epsilon+p)\left(m+4\pi r^3 p\right)}{r(r-2m)} \\ \frac{\mathrm{d}m(r)}{\mathrm{d}r} & = 4\pi r^2 \epsilon \end{cases} \tag{2.1}$$

In this chapter we will discuss the main properties of the EOS that we have used in our calculations. For the description of the low density region (the outer crust) we use the model devised by Baym, Pethick, and Sutherland (BPS) [7]. Since there is relative consensus on the description of the outer crust, the many neutron star models available

on the market differ on their approach towards the inner crust and core. Therefore, we shall not delve into the BPS model but, rather, will highlight some of the properties of the unified model for the inner crust and core that we use here – the $NL3\omega\rho$ model. Lastly, we shall discuss briefly the effects of the inclusion of magnetic field on the crust-core transition region.

2.1 The $\sigma - \omega$ model: an introduction to relativistic mean field models

The NL3$\omega\rho$ model that we use in our calculation is a more sophisticated version of the $\sigma - \omega$, the simplest of the relativistic mean field models. Therefore, we find it pedagogical to discuss it here with some depth, in order to introduce some general techniques that are used in more complicated models and for construction of an equation of state in general. Our discussion follows that of [8], which we recommend for more details.

The $\sigma - \omega$ model is constructed using the fields of 4 particles: the nucleons (protons and neutrons), ψ, a scalar meson, σ, and the omega vector meson, ω_μ. The Lagrangian of the theory is simply the sum of the free Lagrangians of each fields plus the interaction Lagrangian:

$$\mathcal{L} = \mathcal{L}_{nucl} + \mathcal{L}_\sigma + \mathcal{L}_\omega + \mathcal{L}_{int} \quad , \tag{2.2}$$

where,

$$\mathcal{L}_{nucl} = \overline{\psi}\left(\mathrm{i}\partial\!\!\!/ - m\right)\psi, \quad \text{with} \quad \psi \equiv \begin{pmatrix} \psi_p \\ \psi_n \end{pmatrix}, \tag{2.3}$$

$$\mathcal{L}_\sigma = \frac{1}{2}\left(\partial_\mu\partial^\mu\sigma - m_\sigma^2\sigma^2\right) \tag{2.4}$$

$$\mathcal{L}_\omega = -\frac{1}{4}\omega_{\mu\nu}\omega^{\mu\nu} + \frac{1}{2}m_\omega^2\omega_\mu\omega^\mu \tag{2.5}$$

$$\mathcal{L}_{int} = g_\sigma\sigma\overline{\psi}\psi - g_\omega\omega_\mu\overline{\psi}\gamma^\mu\psi. \tag{2.6}$$

In the equations above, all fields are function of x ($x \equiv x^\mu \equiv (t, x, y, z)$). ψ_p and ψ_n are, respectively, the proton and neutron fields. $\omega_{\mu\nu}$ is the tensor defined as $\omega_{\mu\nu} = \partial_\mu \omega_\nu - \partial_\nu \omega_\mu$.

The quantities g_σ and g_ω are the coupling constants of σ and ω^μ to the nucleon fields. m_σ and m_ω are their respective masses, whilst m is related to the mass of the two nucleons:

$$m = \begin{pmatrix} m_p & 0 \\ 0 & m_n \end{pmatrix} \tag{2.7}$$

.

2.1.1 Dynamical equations

The dynamical equations for each field can be obtained from the Euler-Lagrange equation[1]:

$$\partial_\mu \left(\frac{\partial \mathcal{L}}{\partial \left(\partial_\mu \phi \right)} \right) - \frac{\partial \mathcal{L}}{\partial \phi} = 0 \quad , \tag{2.8}$$

where ϕ stands for any of the fields. By doing this we obtain the three following equations:

$$\left(\Box + m_\sigma^2 \right) \sigma \left(x \right) = g_\sigma \overline{\psi} \left(x \right) \psi \left(x \right) \tag{2.9}$$

$$\left(\Box + m_\omega^2 \right) \omega_\mu \left(x \right) - \partial_\mu \partial^\nu \omega_\nu \left(x \right) = g_\omega \overline{\psi} \left(x \right) \gamma_\mu \psi \left(x \right) \tag{2.10}$$

$$\left[\gamma_\mu \left(\partial^\mu + g_\omega \omega^\mu \left(x \right) \right) - \left(m - g_\sigma \sigma \left(x \right) \right) \right] \psi \left(x \right) = 0 \tag{2.11}$$

2.1.2 Mean-field approximation

The mean field approximation consists in replacing the meson fields (in this case σ and ω) by their mean values measured in the ground state:

[1] $\Box$ is the d'Alembertian operator defined as $\Box := \partial_\mu \partial^\mu$.

$$\sigma \to \langle\sigma\rangle \qquad ; \qquad \omega_\mu \to \langle\omega_\mu\rangle.$$

According to Equations (2.9) and (2.10), these values are obtained by solving two differential equations where $\overline{\psi}\psi$ and $\overline{\psi}\gamma^\mu\psi$ act as source currents. In uniform static matter these currents are independent of x and, therefore, the expected values of the meson fields are also independent of x (hereafter we are going to represent these expected values simply as σ and ω_μ). In light of this, the derivatives of the meson fields vanish from their respective dynamical equations:

$$m_\sigma^2 \sigma = g_\sigma \langle\overline{\psi}\psi\rangle \tag{2.12}$$

$$m_\omega^2 \omega_\mu = g_\omega \langle\overline{\psi}\gamma_\mu\psi\rangle \tag{2.13}$$

As for the fermionic fields, the uniform static matter assumption means that we can treat the meson fields appearing in Equation (2.11) simply as constants. By doing so, we see that Equation (2.11) is the Dirac equation with a redefined mass term and a shift in the energy eigenvalue. Therefore, the fermion fields are momentum eigenstates:

$$\psi(x) = \psi(k)\, \mathrm{e}^{-\mathrm{i}k^\mu x_\mu} \quad , \tag{2.14}$$

so that we obtain

$$\left[\gamma_\mu \left(k^\mu + g_\omega \omega^\mu\right) - \left(m - g_\sigma \sigma\right)\right] \psi(k) = 0. \tag{2.15}$$

If we introduce the following definitions

$$\begin{cases} K_\mu = k_\mu - g_\omega \omega_\mu \\ m^*(\sigma) = m - g_\sigma \sigma, \end{cases} \tag{2.16}$$

we can rewrite Equation (2.11) as

$$\left(\not{K} - m^*\right)\psi\left(k\right) = 0 \quad , \tag{2.17}$$

which has a more familiar form. This equation is verified if

$$\left(\not{K} - m^*\right)\left(\not{K} + m^*\right) = 0 \Rightarrow K_0 = \sqrt{\boldsymbol{K}^2 + m^{*2}} \quad . \tag{2.18}$$

With Equations (2.16) and (2.18) we can now write the nucleon eigenvalues for particle and antiparticle :

$$\begin{cases} e\left(\boldsymbol{k}\right) = E\left(\boldsymbol{k}\right) + g_\omega \omega_0 \\ \overline{e}\left(\boldsymbol{k}\right) = E\left(\boldsymbol{k}\right) - g_\omega \omega_0 \end{cases} \quad , \tag{2.19}$$

with

$$E\left(\boldsymbol{k}\right) = \sqrt{\left(\boldsymbol{k} - g_\omega \boldsymbol{\omega}\right)^2 + \left(m - g_\sigma \sigma\right)^2} \quad . \tag{2.20}$$

2.1.3 Evaluating the source currents

In order to calculate the currents that appear in Equation (2.12) and (2.13), one could write the nucleon spinors explicitly and perform the integration. Here we will exemplify a less cumbersome method, which does not require construction of the spinors. This method can also be applied in more complicated models, such as the NL3$\omega\rho$ that we will discuss afterwards.

First we note that a single nucleon state is characterized by the momentum $\boldsymbol{k}$ and its quantum numbers (in this case, the spin and isospin projection), κ. Following the same notation as in [8], we will represent the expectation value of a single-particle state as $\left(\overline{\psi}\Gamma\psi\right)_{\boldsymbol{k}_\kappa}$. The expectation value of this same operator in the ground state of the many-particle system is

$$\langle \overline{\psi}\Gamma\psi \rangle = \sum_{\kappa} \int \frac{\mathrm{d}\boldsymbol{k}}{(2\pi)^3} \left(\overline{\psi}\Gamma\psi \right)_{\boldsymbol{k}_\kappa} \Theta \left[\mu - \epsilon \left(\boldsymbol{k} \right) \right] \quad , \tag{2.21}$$

where Θ is the Heaviside step function and μ is the chemical potential.

The trick consists in finding the single-particle expectation value of any operator from the Hamiltonian. From Equation (2.15) we identify the Dirac Hamiltonian as

$$H_D \equiv k^0 = \gamma^0 \left(\boldsymbol{\gamma k} - g_\omega \gamma_\mu \omega^\mu - m^* \right) \quad . \tag{2.22}$$

The single-particle expectation value of the Hamiltonian is

$$\left(\psi^\dagger H_D \psi \right)_{\boldsymbol{k}_\kappa} = K_0 \left(\boldsymbol{k} \right) = E \left(\boldsymbol{k} \right) + g_\omega \omega_0 \, . \tag{2.23}$$

Derivating by an arbitrary variable of the Hamiltonian ξ we obtain

$$\begin{aligned} \frac{\partial}{\partial \xi} \left(\psi^\dagger H_D \psi \right)_{\boldsymbol{k}_\kappa} &= \left(\psi^\dagger \frac{\partial H_D}{\partial \xi} \psi \right)_{\boldsymbol{k}_\kappa} + k_0 \left(\boldsymbol{k} \right) \frac{\partial}{\partial \xi} \left(\psi^\dagger \psi \right)_{\boldsymbol{k}_\kappa} \\ &= \left(\psi^\dagger \frac{\partial H_D}{\partial \xi} \psi \right)_{\boldsymbol{k}_\kappa} \quad . \end{aligned} \tag{2.24}$$

The second term in Equation (2.24) vanishes because $\psi \left(\boldsymbol{k} \right)$ is an eigenfunction. Our task is now to find the right ξ such that $\frac{\partial H_D}{\partial \xi} = \Gamma$.

For example, if we wanted to calculate $\langle \psi^\dagger \psi \rangle$, then ξ should be ω_0. In this case,

$$\begin{aligned} & \frac{\partial}{\partial \omega_0} \left(\psi^\dagger H_D \psi_{\boldsymbol{k}_\kappa} \right) = \left(\psi^\dagger \frac{\partial H_D}{\partial \omega_0} \psi \right)_{\boldsymbol{k}_\kappa} \\ \Leftrightarrow \quad & g_\omega = \left(\psi^\dagger \frac{\partial H_D}{\partial \omega_0} \psi \right)_{\boldsymbol{k}_\kappa} \\ \Leftrightarrow \quad & g_\omega = \left(\psi^\dagger g_\omega \psi \right)_{\boldsymbol{k}_\kappa} \\ \Leftrightarrow \quad & \left(\psi^\dagger \psi \right)_{\boldsymbol{k}_\kappa} = 1 \quad , \end{aligned} \tag{2.25}$$

and, from Equation (2.21), we obtain the baryon density:

$$\rho = \langle \psi^\dagger \psi \rangle = 4 \int_0^{\boldsymbol{k}} \frac{\mathrm{d}\boldsymbol{k}}{(2\pi)^3} \Theta \left[\mu - \epsilon \left(\boldsymbol{k} \right) \right] \quad . \tag{2.26}$$

The calculation of other expectation values are not so trivial, but they follow the same procedure. In the end we obtain

$$\begin{cases} \langle \overline{\psi} \gamma^i \psi \rangle = 4 \int \frac{\mathrm{d}k^i \mathrm{d}k^j \mathrm{d}k^k}{(2\pi)^3} \left(\frac{\partial}{\partial k^i} E \left(\boldsymbol{k} \right) \right) \Theta \left(\mu - \epsilon \left(\boldsymbol{k} \right) \right) = 0, \quad \text{repeated indices do not imply sum} \\ \langle \overline{\psi} \psi \rangle \equiv \rho_s = \frac{2}{\pi} \int_0^k k^2 \mathrm{d}k \frac{m - g_\sigma \sigma}{\sqrt{k^2 + (m - g_\sigma \sigma)^2}} \\ \langle \psi^\dagger \psi \rangle \equiv \rho = 4 \int_0^k \frac{4\pi k^2 \, \mathrm{d}k}{(2\pi)^3} = \frac{2k^3}{3\pi^2} \end{cases} \tag{2.27}$$

2.1.4 Obtaining the equation of state

The results that we obtained for the source currents allow us to rewrite the dynamical equations for the meson fields as

$$\begin{cases} g_\sigma \sigma = \left(\frac{g_\sigma}{m_\sigma} \right)^2 \frac{2}{\pi^2} \int_0^k k^2 \mathrm{d}k \frac{m - g_\sigma \sigma}{\sqrt{k^2 + (m - g_\sigma \sigma)}} \\ g_\omega \omega_0 = \left(\frac{g_\omega}{m_\omega} \right)^2 \rho \\ m_\omega^2 \omega_k = 0 \end{cases} \tag{2.28}$$

In order to obtain the equation of state we are going to write the energy density, ϵ, and pressure, p as function of parameters of the model. We achieve this by first computing the energy-momentum tensor from the Lagrangian that describes our model:

$$T^{\mu\nu} = \frac{\partial \mathcal{L}}{\partial \left(\partial_\mu \phi \right)} - \eta^{\mu\nu} \mathcal{L}, \tag{2.29}$$

where ϕ stands for each of the fields in our theory. We model the stellar matter as a perfect fluid, thus the energy-momentum tensor can also be written as

$$T^{\mu\nu} = -p\eta^{\mu\nu} + (p+\epsilon)\, u^{\mu}u^{\nu}\,. \tag{2.30}$$

The expressions for ϵ and p are obtained by equating Equation (2.29) with Eq. (2.30):

$$\epsilon = -\langle\mathcal{L}\rangle + \langle\overline{\psi}\gamma_0 k_0\psi\rangle \tag{2.31}$$

$$p = \langle\mathcal{L}\rangle + \frac{1}{3}\langle\overline{\psi}\gamma_i k_i\psi\rangle \tag{2.32}$$

After calculating the expectation values in Equations (2.31) and (2.32) we obtain the integral equations for ϵ and p, which, together, form our equation of state.

2.2 The NL3$\omega\rho$ model

The model that we are going to use in our calculations includes a series of improvements over the $\omega - \rho$ [9]. The NL3$\omega\rho$ model satisfies a series of experimental constraints for nuclear matter [10], including those of the recent gravitational waves event GW170817 [11]. First, the Lagrangian of the scalar field σ is modified to include self-interaction terms, as proposed by [12]. This allows a better description of the compression modulus and nucleon effective mass at saturation density. These self-interaction terms are associated with the coupling constants κ and λ.

$$\mathcal{L}_\sigma = \frac{1}{2}\left(\partial_\mu\sigma\partial^\mu\sigma - m_\sigma^2\sigma^2\right) - \frac{\kappa}{3!}\sigma^3 - \frac{\lambda}{4!}\sigma^4 \tag{2.33}$$

We also include a new field – the $\boldsymbol{\rho}^{\mu}$ meson – which allows for a better description of nuclear asymmetric matter [8]:

$$\mathcal{L}_\rho = -\frac{1}{4}\boldsymbol{B_{\mu\nu}B^{\mu\nu}} + \frac{1}{2}m_\rho^2\boldsymbol{\rho_\mu\rho^\mu} \quad , \tag{2.34}$$

where

$$\boldsymbol{B^{\mu}} = \partial^{\mu}\boldsymbol{\rho^{\nu}} - \partial^{\nu}\boldsymbol{\rho^{\mu}} - g_{\rho}\left(\boldsymbol{\rho^{\mu}} \times \boldsymbol{\rho^{\nu}}\right) \quad , \tag{2.35}$$

and g_ρ is a constant. The field $\boldsymbol{\rho^{\mu}}$ is a three component vector field, $\boldsymbol{\rho^{\mu}} = (\rho_1^{\mu}, \rho_2^{\mu}, \rho_3^{\mu})$, whose components share the same mass, but have different isospin charges $(\pm 1, 0)$. Although, as discussed in [8], only the 0-isospin component, ρ_3^{μ}, is relevant for the description of the ground state, since the components have vanishing mean values.

The $\omega - \rho$ term, from which the model gets its name, is introduced to improve the description of the density dependence of the symmetry energy above the saturation density [13]:

$$\mathcal{L}_{\omega\rho} = \Lambda_{\omega\rho} g_{\omega}^2 g_{\rho}^2 \left(\boldsymbol{\rho_{\lambda}} \cdot \boldsymbol{\rho^{\lambda}}\right) \left(\omega_{\mu}\omega^{\mu}\right) . \tag{2.36}$$

Finally, we include the contribution of the electrons, whose importance in the description of the stellar matter was noted by [14]:

$$\mathcal{L}_e = \overline{\psi}\left[\gamma_{\mu}\left(\mathrm{i}\partial^{\mu} + eA^{\mu}\right) - m_e\right]\psi_e \, . \tag{2.37}$$

In this model the mass matrix of the nucleons must be change to $m^* = m - g_\sigma\sigma$. Plus, the derivative operator that appears in the nucleon Lagrangian must be replaced by the following covariant derivative:

$$\mathrm{i}D^{\mu} = \mathrm{i}\partial^{\mu} - g_{\omega}\omega^{\mu} - \frac{g_{\rho}}{2}\boldsymbol{\tau} \cdot \boldsymbol{\rho^{\mu}} - \mathrm{e}A^{\mu}\frac{1+\tau_3}{2} \quad , \tag{2.38}$$

where e stands for the electron charge and $\boldsymbol{\tau} = (\tau_1, \tau_2, \tau_3)$ is the vector containing the Pauli matrices:

$$\tau_1 = \begin{pmatrix} 0 & 1 \\ 1 & 0 \end{pmatrix}; \quad \tau_1 = \begin{pmatrix} 0 & -\mathrm{i} \\ \mathrm{i} & 0 \end{pmatrix}; \quad \tau_1 = \begin{pmatrix} 1 & 0 \\ 0 & -1 \end{pmatrix} . \tag{2.39}$$

The full Lagrangian of the theory is going to be the sum of all contributions that we have discussed above and the construction of the equation of state follows the same techniques exemplified for the $\sigma - \omega$ model.

$$\mathcal{L} = \mathcal{L}_{nucl} + \mathcal{L}_{\sigma} + \mathcal{L}_{\omega} + \mathcal{L}_{\boldsymbol{\rho}} + \mathcal{L}_{\omega\rho} + \mathcal{L}_{e} \tag{2.40}$$

It is important to note that we do not include the purely electromagnetic contribution $\mathcal{L}_A = -\frac{1}{4}F_{\mu\nu}F^{\mu\nu}$ on the equations of state that we use in our LORENE simulations. However, this contribution is important when we study the instability region of the inner crust, as we discuss next.

In this work we focus on two parameterizations of the NL3$\omega\rho$ model: one with the value of the slope of the symmetry energy, L, equal to 55 MeV and another with $L = 88$ MeV. The parameters for each case are presented in Table 2.1.

Table 2.1: Parameters of the NL3$\omega\rho$ model.

Parameter	Value
m_σ (MeV)	508.194
m_ω (MeV)	782.5
m_ρ (MeV)	763
g_σ	10.217
g_ω	12.868
κ (fm^{-1})	20.868
λ	-173.31
g_ρ, for $L = 55$ MeV	11.2756
g_ρ, for $L = 88$ MeV	9.5363
$g_{\omega\rho}$, for $L = 55$ MeV	0.03
$g_{\omega\rho}$, for $L = 88$ MeV	0.01

2.3 Inner crust: collective modes and instability region

In this section we summarize the method described in [2], and based on the formalism discussed in [15], that allows for the calculation of the crust-core transition region taking in account the effects of strong magnetic fields. In a nutshell, this is achieved by considering small oscillations around the equilibrium state of the fermion and meson fields; the dispersion relation of the resulting collective modes is then obtained from an eigenvalue problem; the spinodal section for a given wave vector $\boldsymbol{k}$ corresponds to the region of the space (ρ_p, ρ_n) for which $\omega = 0$, where ω is an eigenmode.

We will consider the same model described by the Lagrangian in Eq.(2.33), except that now we include the purely electromagnetic contribution $\mathcal{L}_A$:

$$\mathcal{L} = \mathcal{L}_{nucl} + \mathcal{L}_\sigma + \mathcal{L}_\omega + \mathcal{L}_{\boldsymbol{\rho}} + \mathcal{L}_{\omega\rho} + \mathcal{L}_e + \mathcal{L}_A/, . \tag{2.41}$$

We will consider a static electromagnetic field with $A^\mu = (0, 0, Bx, 0)$, so that $\boldsymbol{B} = B\hat{\boldsymbol{z}}$ and $\boldsymbol{\nabla} \cdot \boldsymbol{B} = 0$. In the presence of a magnetic field, the nucleon Lagrangian becomes

$$\mathcal{L}_{nucl} = \overline{\psi}_i \left[\gamma_\mu \mathrm{i} D^\mu - m^* - \frac{1}{2} \mu_N \kappa_b \sigma_{\mu\nu} F^{\mu\nu} \right] \psi, \tag{2.42}$$

where μ_N is the nuclear magneton and $\sigma = \frac{\mathrm{i}}{2} [\gamma_\mu, \gamma_\nu]$. κ_b mesures the strenght of the interaction of the nucleons (b stands for either n or p) with the anomalous magnetic moment (AMM).

In this formalism, the composition of matter is described by a distribution function:

$$f(\boldsymbol{r}, \boldsymbol{p}, t) = \mathrm{diag}(f_p, f_n, f_e) \quad , \tag{2.43}$$

where the labels p, n and e stand, respectively, for proton, neutron and electron. The distribution function is defined as a function whose integral over the phase space gives the number density of particle, i.e.,

$$n_i(\boldsymbol{r},t) = \frac{1}{(2\pi)^3}\int f_i \mathrm{d}^3\boldsymbol{p} \quad ; \quad \mathrm{i} = \mathrm{n,p,e}. \tag{2.44}$$

The distribution function obeys the following evolution equation (Vlasov equation):

$$\frac{\partial f_i}{\partial t} + \{f_i, h_i\} = 0 \quad \mathrm{i} = \mathrm{n,p,e}, \tag{2.45}$$

where $\{,\}$ denotes the Poisson brackets and h is the one body Hamiltonian defined as $h = \mathrm{diag}\,(h_p, h_n, h_e)$. As consequence of inclusion of the magnetic field, these quantities are quantized [16] [17]:

$$h_i = \epsilon_i + \mathcal{V}_0^i, \quad \epsilon_i = \sqrt{\left(\overline{\boldsymbol{p}}_z^i\right)^2 + \overline{m}_i^2}, \quad \mathrm{i} = \mathrm{p,e} \tag{2.46}$$

$$h_n = \epsilon_n + \mathcal{V}_0^n, \quad \epsilon_n = \sqrt{\left(\overline{\boldsymbol{p}}_z^n\right)^2 + \left(\epsilon_\perp^n - s\mu_N k_n B\right)^2} \tag{2.47}$$

where we have introduced the following definitions:

$$\overline{\boldsymbol{p}}^i = \boldsymbol{p} - \boldsymbol{\mathcal{V}}^i, \tag{2.48}$$

$$\mathcal{V}_\mu^n = g_\omega \omega_\mu - \frac{g_\rho}{2}\rho_\mu, \tag{2.49}$$

$$\mathcal{V}_\mu^p = g_\omega \omega_\mu + \frac{g_\rho}{2}\omega_\mu + \mathrm{e}A_\mu, \tag{2.50}$$

$$\mathcal{V}_\mu^\mathrm{e} = -\mathrm{e}A_\mu, \tag{2.51}$$

$$\overline{m}_p = \sqrt{m^{*2} + 2\nu \mathrm{e}B} - s\mu_N \kappa_p B, \tag{2.52}$$

$$\overline{m}_\mathrm{e} = \sqrt{m_\mathrm{e}^{*2} + 2\nu \mathrm{e}B}, \tag{2.53}$$

$$\bar{\epsilon}_\perp^n = \sqrt{m^{*2} + \left(\overline{\boldsymbol{p}}_\perp^n\right)^2}. \tag{2.54}$$

The discrete character of the Hamiltonian is introduced via the quantity $\nu = n + \frac{1}{2} - sgn\,(q)\,\frac{s}{2} = 0, 1, 2, \ldots$, which enumerates the Landau levels of the fermions with electric charge q, and spin projection s (along the direction of the magnetic field, $\hat{\boldsymbol{z}}$).

As before, the evolution equations for the fields are obtained from Euler-Lagrange equations:

$$\frac{\partial^2\phi}{\partial t^2} - \nabla^2\phi + m_\sigma^2\phi + \frac{\kappa}{2}\phi^2 + \frac{\lambda}{6}\phi^3 = g_s\left[\rho_s^p + \rho_s^n\right], \tag{2.55}$$

$$\frac{\partial^2\omega_\mu}{\partial t^2} - \nabla^2\omega_\mu + m_\omega^2\omega_\mu + 2\Lambda_\omega g_\omega^2 g_\rho^2 \rho_{3\mu}\rho^{3\mu}\omega_\mu = g_\omega\left[j_\mu^p + j_\mu^n\right], \tag{2.56}$$

$$\frac{\partial^2\rho_{3\mu}}{\partial t^2} - \nabla^2\rho_{3\mu} + m_\rho^2\rho_{3\mu} + 2\Lambda_\omega g_\omega^2 g_\rho^2 \omega_\mu\omega^\mu\rho_{3\mu} = \frac{g_\rho}{2}\left[j_\mu^p - j_\mu^n\right], \tag{2.57}$$

$$\frac{\partial^2 A_\mu}{\partial t^2} - \nabla^2 A_\mu = \mathrm{e}\left[j_\mu^p - j_\mu^{\mathrm{e}}\right], \tag{2.58}$$

where the scalar densities and source currents for the fields are given by the following expressions:

$$\rho_s^p(\boldsymbol{r},t) = \frac{\mathrm{e}B}{(2\pi)^2}\sum_{\nu,s}\int \mathrm{d}p_z f_p \frac{\overline{m}_p m^*}{\left(\overline{m}_p + s\mu_N\kappa_p B\right)\epsilon_p}, \tag{2.59}$$

$$\rho_s^n(\boldsymbol{r},t) = \frac{1}{(2\pi)^3}\sum_{s}\int \mathrm{d}^3p f_n\left(1 - \frac{s\mu_N\kappa_n B}{\sqrt{m^{*2}+p_\perp^2}}\right)\frac{m^*}{\epsilon_n} \tag{2.60}$$

$$j_0^i(\boldsymbol{r},t) = \rho_i = \frac{\mathrm{e}B}{(2\pi)^2}\sum_{\nu,s}\int f_i(\boldsymbol{r},\boldsymbol{p},t)\,\mathrm{d}p_z, \quad \mathrm{i} = \mathrm{p},\mathrm{e}, \tag{2.61}$$

$$j_0^n(\boldsymbol{r},t) = \rho_n = \frac{1}{(2\pi)^3}\sum_{s}\int f_n(\boldsymbol{r},\boldsymbol{p},t)\,\mathrm{d}^3p, \tag{2.62}$$

$$\boldsymbol{j}^i(\boldsymbol{r},t) = \frac{\mathrm{e}B}{(2\pi)^2}\sum_{\nu,s}\int f_i(\boldsymbol{r},\boldsymbol{p},t)\,\frac{\overline{\boldsymbol{p}}_z^i}{\epsilon_i}\mathrm{d}p_z, \quad \mathrm{i} = \mathrm{p},\mathrm{e}, \tag{2.63}$$

$$\boldsymbol{j}^n(\boldsymbol{r},t) = \frac{1}{(2\pi)^3}\sum_{s}\int f_n(\boldsymbol{r},\boldsymbol{p},t)\,\mathrm{d}^3p \times \left[\frac{\overline{\boldsymbol{p}}_z^n}{\epsilon_n} + \frac{\overline{\boldsymbol{p}}_\perp^n}{\epsilon_n}\left(1 - \frac{s\mu_N\kappa_n B}{\sqrt{m^{*2}+\left(\overline{\boldsymbol{p}}_\perp^n\right)^2}}\right)\right] \tag{2.64}$$

The ground state at zero temperature is characterized by the neutron, proton and electron Fermi momenta, $P_F^i\,(i = \mathrm{p},\mathrm{n},\mathrm{e})$, and the distribution function (Equation (2.43)) now reads

$$f_0(\boldsymbol{r},\boldsymbol{p}) = \mathbf{diag}\left[\Theta\left(P_F^{p2} - p^2\right), \Theta\left(P_F^{n2} - p^2\right), \Theta\left(P_F^{\mathrm{e}2} - p^2\right)\right], \tag{2.65}$$

where

$$P_F^p = \sqrt{\epsilon_F^p - \overline{m}_p^2}, \tag{2.66}$$

$$P_F^n = \sqrt{\gamma - \sqrt{\gamma^2 - \beta}}, \tag{2.67}$$

$$P_F^{\mathrm{e}} = \sqrt{\epsilon_F^{\mathrm{e}} - \overline{m}_{\mathrm{e}}^2}, \tag{2.68}$$

with

$$\gamma = \alpha + 2\left(s\mu_N\kappa_n B\right)^2\left(1 - x^2\right), \tag{2.69}$$

$$\alpha = \epsilon_F^{n2} - m^{*2} - \left(s\mu_N\kappa_n B\right)^2, \tag{2.70}$$

$$\beta = \alpha^2 - 4\left(s\mu_N\kappa_n B\right)^2 m^{*2} \tag{2.71}$$

In Equation (2.69), $x = \cos\theta'$, where θ' is the polar angle. In the ground state the evolution equations (2.55) – (2.58) reduce into the followings:

$$\begin{cases} m_s^2\phi_0 + \frac{\kappa}{2}\phi_0^2 + \frac{\lambda}{6}\phi_0^3 = g_\sigma\rho_s^{(0)}, \\ m_\omega^2\omega_0^{(0)} + 2\Lambda_\omega g_\omega^2 g_\rho^2\omega_0^{(0)}\rho_0^{(0)2} = g_\omega j_0^{(0)}, \\ m_\rho^2\rho_0^{(0)} + 2\Lambda_\omega g_\omega^2 g_\rho^2\omega_0^{(0)2}\rho_0^{(0)} = \frac{g_\rho}{2} j_{3,0}^{(0)}, \\ \omega_i^{(0)} = \rho_i^{(0)} = A_0^{(0)} = A_i^{(0)} = 0, \end{cases} \tag{2.72}$$

where $\rho_s^{(0)}$, $j_{3,0}^{(0)}$ and $j_0^{(0)}$ are the corresponding scalar density, nuclear density and isospin density, respectively. In the equations above, and throughout the rest of this chapter, we have omit the subscript labelling the third component of the $\boldsymbol{\rho}^\mu$ field.

The collective modes are obtained by considering small deviations from the equilibrium state:

$$\begin{cases} f_i = f_{0i} + \delta f_i, \\ \phi = \phi_0 + \delta\phi, \\ \omega_0 = \omega_0^{(0)} + \delta\omega_0, \quad \omega_i = \delta\omega_i, \\ \rho_{3\,0} = \rho_{3\,0}^{(0)} + \delta\rho_{3\,0}, \quad \rho_{3\,i} = \delta\rho_{3\,i}, \\ A_0 = A_0, \quad A_i = \delta A_i. \end{cases} \tag{2.73}$$

The fluctuations δf_i are obtained from a generating function $S(\boldsymbol{r}, \boldsymbol{p}) = \mathbf{diag}(S_p, S_n, S_e)$ in the following way:

$$\delta f_i = \{S_i, f_{0\,i}\} = -\{S_i, p^2\}\delta\left(P_F^{i2} - p2\right). \tag{2.74}$$

The components of the generating function S_i obey the following evolution equation [18] :

$$\frac{\partial S_i}{\partial t} + \{S_i, h_{0i}\} = \delta h_i, \quad \mathrm{i} = \mathrm{p}, \mathrm{n}, \mathrm{e}, \tag{2.75}$$

where h_i are the one-body Hamiltonians for the proton, neutron and electron states at equilibrium.

We are going to consider longitudinal perturbations with momentum $\boldsymbol{k}$, along the direction of the magnetic field, and frequency ω. This can be introduced through the following ansatz:

$$\begin{pmatrix} S_j(\boldsymbol{r}, \boldsymbol{p}, r) \\ \delta\phi \\ \delta\xi_0 \\ \delta\xi_i \end{pmatrix} = \begin{pmatrix} S_\omega^j(p, \cos\theta) \\ \delta\phi_\omega \\ \delta\xi_{0\,\omega} \\ \delta\xi_{i\,\omega} \end{pmatrix} \mathrm{e}^{(\omega t - \boldsymbol{k}\boldsymbol{r})}; \quad \mathrm{j} = \mathrm{p}, \mathrm{n}, \mathrm{e}, \tag{2.76}$$

where $\mathrm{j} = \mathrm{p}, \mathrm{n}, \mathrm{e}$, ξ stands for each of the vector fields ($\xi = \omega, \rho^\mu, A$) and θ is the angle between $\boldsymbol{p}$ and $\boldsymbol{k}$.

With this ansatz, $\delta\omega_{x\,\omega} = \delta\omega_{y\,\omega} = 0$, $\delta\rho_{x\,\omega} = \delta\rho_{y\,\omega} = 0$ and $\delta A_{x\,\omega} = \delta A_{y\,\omega} = 0$. Therefore we can simplify the notation by calling $\delta\omega_{z\,\omega} = \delta\omega_\omega$, $\delta\rho_{z\,\omega} = \delta\rho_\omega$ and $\delta A_{z\,\omega} = \delta A_\omega$.

Replacing the ansatz into Equation (2.75) we obtain a set of 7 evolution equations for each of the components of $S(\boldsymbol{r}, t)$ and for the scalar and vector fields [2]. This set of equations can be rearranged into a set of 5 independent equations of motion in terms of the amplitudes of the proton and neutron scalar density fluctuations, $A^{ps}_{\omega,\nu,s}$ and $A^{ns}_{\omega,s}$, and in terms of the amplitudes of the proton, neutron and electron vector density fluctuations, $A^{p}_{\omega,\nu,s}$, $A^{n}_{\omega,s}$, $A^{e}_{\omega,\nu,s}$, respectively.

The set of 5 equations for the amplitudes of the scalar and vector density fluctuations can be written in a matrix form [2]:

$$\begin{pmatrix} a_{11} & a_{12} & a_{13} & a_{14} & a_{15} \\ a_{21} & a_{22} & a_{23} & a_{24} & a_{25} \\ a_{31} & a_{32} & a_{33} & a_{34} & 0 \\ a_{41} & a_{42} & a_{43} & a_{44} & 0 \\ 0 & a_{52} & 0 & 0 & a_{55} \end{pmatrix} \begin{pmatrix} \sum_{\nu,s} A^{ps}_{\omega,\nu,s} \\ \sum_{\nu,s} A^{p}_{\omega,\nu,s} \\ \sum_{s} A^{ns}_{\omega,s} \\ \sum_{s} A^{n}_{\omega,s} \\ \sum_{\nu,s} A^{e}_{\omega,\nu,s} \end{pmatrix} = 0 \tag{2.77}$$

The dispersion relation for the collective modes are then obtained by equating the determinant of the coefficients matrix to zero.

The density fluctuation of each species can be written in terms of respective amplitudes in the following way:

$$\begin{cases} \frac{\delta\rho_n}{\delta\rho_p} = \frac{A^{n}_{\omega,s}}{\mathrm{e}BA^{p}_{\omega,\nu,s}}, \\ \frac{\delta\rho_e}{\delta\rho_p} = \frac{A^{e}_{\omega,\nu,s}}{A^{p}_{\omega,\nu,s}}. \end{cases} \tag{2.78}$$

The set of points in the (ρ_p, ρ_n) space, for a given $\boldsymbol{k}$, for which $\omega = 0$ constitutes the dynamical spinodal surface. This surface defines the frontier of stable (outside the surface) and unstable (inside the surface) matter. The inclusion of strong magnetic fields induces the comb-like pattern of the spinodal surface (Figure 2.1), which is associated with the Landau levels of the energy eigenvalues.

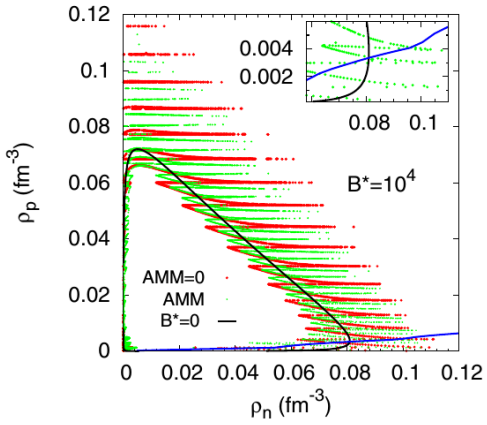

Figure 2.1: Dynamical spinodal for NL3$\omega\rho$, a moment transfer of $k = 75$ MeV, with AMM (green) and without AMM (red) , for $B = 4.41 \times 10^{17}$ G. The β equilibrium curve is represented in blue. Figure taken from [2]

As we said before, we are interested in this formalism to calculate the crust-core transition taking into account the effects of magnetic fields. The densities at which this transition occurs is given by the intersection of the (ρ_p, ρ_n) curve at β equilibrium with the spinodal. For $B = 0$ this intersection corresponds to a single point, as can be seen in Figure 2.1, where the spinodal for $B = 0$ is represented by a black line. For $B \neq 0$, we can see that the β equilibrium line crosses the spinodal (green lines for calculations with anomalous magnetic moment, AMM, and red lines without AMM) multiple times before reaching a zone where there are no more intersections. Physically, this means that before one reaches a zone of stable matter, there is an intermediate region where stable and unstable matter interchange (cf. Figure 2.2) . We call this region the extended crust-core transition zone. Throughout this work ρ_1 stands for the lower bound of this region and ρ_2 stands for the upper bound.

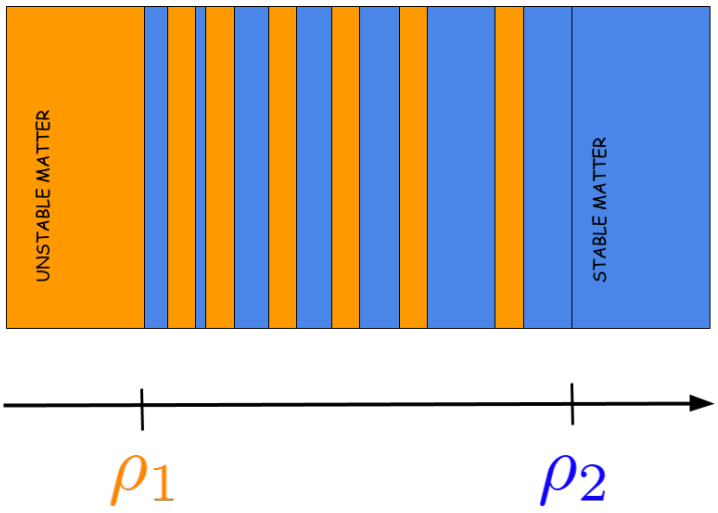

Figure 2.2: Extended crust-core transition zone.

Chapter 3

Numerical Relativity

The challenges of solving Einstein's equations on a computer arise from two directions. First, Einstein's equations are a set of 10 coupled nonlinear differential equations and, as such, there is not an unified framework to deal with every problem [19]. However, this feature is not particular to Einstein's equations, but it is shared by many other equations encountered in physical theories, the Navier-Stokes's equation being, perhaps, the most famous case.

The most peculiar feature of Einstein's equations arises from the geometrical nature of the theory. The problem of solving Einstein's equations can be stated as finding the components of the metric tensor, $g_{\mu\nu}$, for the given energy-momentum tensor $T_{\mu\nu}$. But in order to work with the components of the metric tensor one has to choose some coordinate system and, thus, the components $g_{\mu\nu}$ are sensible to change of coordinates. Since there are four spacetime coordinates, there are also four arbitrary degrees of freedom to ten $g_{\mu\nu}$ and, for that reason, it should be impossible to determine all ten $g_{\mu\nu}$ from any initial data – the coordinates to the future of the initial moment can be changed arbitrarily [20]. This property is expressed by the Bianchi identities

$$G^{\mu\nu}_{;\beta} = 0, \tag{3.1}$$

where $G^{\mu\nu}$ stands for the Einstein tensor. The Bianchi identities imply that there are are only six independent differential equations among the ten $G^{\mu\nu}$.

The properties of the Einstein's equations discussed above do not prevent one from solving these equations numerically in the form of a well posed initial-value problem. Instead it only means that in order to solve General Relativity numerically, one has to construct a framework in which the coordinate freedom in $g_{\mu\nu}$ does not spoil the evolution scheme from an initial set of conditions. This can be achieved by treating space and time coordinates as they were independent from each other. In LORENE this is implemented according to the $3+1$ formalism, which we will briefly discuss in this chapter.

3.1 Einstein's equations in a brief

In this section we summarize the main results of the theory of general relativity that are going to be relevant for our discussion. We are going to use units such that $G = 1$ and the $\{-+++\}$ convention for the Minkowski metric. Throughout this chapter greek indices run from $0-3$, whilst roman indices go from $1-3$.

The essence of the theory of general relativity is all condensed in the form of Einstein's equations:

$$G^{\alpha\beta} = 8\pi T^{\alpha\beta}, \tag{3.2}$$

where $G^{\alpha\beta}$ are the components or the Einstein tensor and $T^{\alpha\beta}$ the components of the energy-momentum tensor.

The Einstein tensor is a symmetric tensor defined as

$$G^{\alpha\beta} \equiv R^{\alpha\beta} - \frac{1}{2} g^{\alpha\beta} R, \tag{3.3}$$

where $g^{\alpha\beta}$ are the components of the metric tensor and R is called the Ricci scalar, also constructed from elements of the metric tensor and its derivatives. Therefore, the left-hand side of Equation (3.2) contains the information regarding the curvature of spacetime, whereas the right-hand side describes the energy source responsible for such curvature.

The Ricci scalar is the result of the contraction of the Riemann tensor:

$$R := g^{\mu\nu} R_{\mu\nu} = g^{\mu\nu} g^{\alpha\beta} R_{\alpha\mu\beta\nu}. \tag{3.4}$$

The Riemann curvature tensor is defined in the following way:

$$R^{\alpha}_{\beta\mu\nu} = \Gamma^{\alpha}_{\beta\mu,\nu} - \Gamma^{\alpha}_{\beta\mu,\nu} + \Gamma^{\alpha}_{\sigma\mu}\Gamma^{\sigma}_{\beta\nu} - \Gamma^{\alpha}_{\sigma\nu}\Gamma^{\sigma}_{\beta\mu}, \tag{3.5}$$

where we have introduced the Christoffel symbols:

$$\Gamma^{\alpha}_{\mu\nu} = \frac{1}{2} g^{\alpha\beta} \left(g_{\beta\mu,\nu} + g_{\beta\nu,\mu} - g_{\mu\nu,\beta} \right). \tag{3.6}$$

3.2 3+1 Formalism

The $3 + 1$ formalism is the most common approach to numerical relativity and it consists in decomposing the four-dimensional spacetime into three-dimensional surfaces (*hypersurfaces*) [21]. Other approaches include the $2 + 2$ formalism [22], the conformal field equations [23] , as well as other approaches applied particularly in black hole mergers [24, 25]. Our discussion of this topic follows closely that presented in [21].

Foliation of spacetime

The spacetime of general relativity is a 4-dimension manifold, i.e., a topological space such that around each point there is a neighbourhood which is homeomorphic to an open subset of $\mathbb{R}^4$. In the $3+1$ formalism, this manifold, $\mathcal{M}$, is sliced by a family of hypersurfaces $(\Sigma_t)_{t\in\mathbb{R}}$:

$$\mathcal{M} = \bigcup_{t\in\mathbb{R}} \Sigma_t, \tag{3.7}$$

with $\Sigma_t \cap \Sigma_{t'} = \emptyset$ for $t \neq t'$. The hypersurfaces (Σ_t) are 3-dimensional submanifolds of $\mathcal{M}$, and every vector in it (i.e, tangent to it) is spacelike. Only the so-called *globally hyperbolic spacetimes* allow for such type of decomposition, but this class encompasses many of the spacetimes generated by compact stars [21].

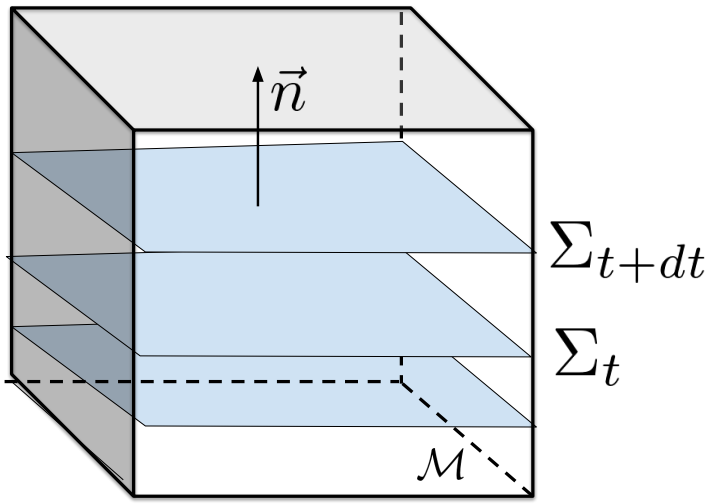

Figure 3.1: $3+1$ decomposition of the four-dimensional spacetime.

Each hypersurface Σ_t is labelled by a parameter t which we identify as a time coordinate. t is a scalar field on $\mathcal{M}$ such that $\langle \nabla, \vec{v} \rangle = 0$ for any vector $\vec{v}$ tangent to Σ_t. Equivalently, the vector $\vec{\nabla} t$ associated with the 1-form [1] ∇t is normal to Σ_t, i.e,

[1] The vector whose components are $\nabla^\alpha t = g^{\alpha\beta}\nabla_\beta t$

$\vec{\nabla}t \cdot \vec{v} = 0$, for all $\vec{v}$ tangent to Σ_t. The association of our scalar field, t, with the time coordinate is made by requiring that $\partial_\alpha t = \delta^0_\alpha$. Since every hypersurfaces is equipped with its own time, the arrow of time can be identified with the unit timelike normal vector $\vec{n}$:

$$\vec{n} \cdot \vec{n} = -1. \tag{3.8}$$

Since $\vec{\nabla}t$ is also normal to Σ_t, we have that:

$$\vec{n} = -N\vec{\nabla}t, \tag{3.9}$$

where N is a proportionality coefficient called the **lapse function**. The minus sign is chosen so that $N \geq 0$ if the scalar field t is increasing towards the time.

If $\boldsymbol{g}$ is the metric function on $\mathcal{M}$, then one can construct a metric function for each of the hypersurfaces Σ_t. This metric, $\boldsymbol{\gamma}$, is the restriction of $\boldsymbol{g}$ on Σ_t (i.e, the metric induced by $\boldsymbol{g}$ onto Σ_t), and it is definite positive [2]:

$$\forall \vec{v} \in \mathcal{T}_p\left(\Sigma_t\right), \quad \vec{v} \neq 0 \implies \gamma\left(\vec{v}, \vec{v}\right) > 0. \tag{3.10}$$

The components of the induced tensor $\boldsymbol{\gamma}$, in terms of the components of $\boldsymbol{g}$, are

$$\gamma_{\alpha\beta} = g_{\alpha\beta} + n_\alpha n_\beta. \tag{3.11}$$

On the other hand, the tensor γ^α_β acts as the orthogonal projector onto Σ_t, which we denote by $\vec{\gamma}$:

$$\gamma^\alpha_\beta = \delta^\alpha_\beta + n^\alpha n_\beta. \tag{3.12}$$

[2] In Eq. (3.10), $\mathcal{T}_p\left(\Sigma_t\right)$ denotes the tangent space of Σ_t at the point p, i.e., the set of all tangent vector of Σ_t at p.

Eulerian observer

We call by **Eulerian observers** or **zero angular-momentum observers (ZAMO)**,the set of observers whose 4-velocity is $\vec{n}$. The wordlines of these observers are the field lines of $\vec{n}$ and are orthogonal to the hypersurfaces Σ_t.

The time measured by a ZAMO is

$$\mathrm{d}\tau = N\mathrm{d}t, \tag{3.13}$$

and its acceleration is given by [26]:

$$\vec{a} = \nabla_{\vec{n}}\vec{n} = \vec{\gamma}\left(\vec{\nabla}\ln N\right). \tag{3.14}$$

The energy-density E, the momentum-density $\vec{p}$ and the stress tensor $\vec{S}$, as measured by the ZAMO are given by:

$$E = T_{\alpha\beta}n^{\alpha}n^{\beta} \tag{3.15}$$

$$p_{\alpha} = -T_{\mu\nu}u^{\nu}\gamma^{\mu}_{\alpha} \tag{3.16}$$

$$S_{\alpha\beta} = T_{\mu\nu}\gamma^{\mu}_{\alpha}\gamma^{\nu}_{\beta}. \tag{3.17}$$

With the above results, the energy-momentum tensor in the $3+1$ decomposition reads:

$$T_{\alpha\beta} = En_{\alpha}n_{\beta} + p_{\alpha}n_{\beta} + n_{\alpha}p_{\beta} + S_{\alpha\beta}. \tag{3.18}$$

Adapted coordinates

A coordinate system $\{x^{\alpha}\}$ is said to be adapted to the foliation $(\Sigma_t)_{t\in\mathbb{R}}$ if and only if $x^0 = t$ [21]. The remaining coordinates (the spatial coordinates) $\{x^i\}$ constitute the coordinate system in Σ_t. The set of vectors $\{\vec{\partial}_t\}$ form a basis in $\mathcal{T}_p\mathcal{M}$ called the natural

basis. In a $3+1$ structure this basis is decomposed into a part along $\vec{n}$ and another tangent to Σ_t:

$$\vec{\partial}_t = N\vec{n} + \vec{\beta} \quad \text{with} \quad \vec{n} \cdot \vec{\beta} = 0. \tag{3.19}$$

The spacelike vector $\vec{\beta}$ is called the **shift vector** and it has only spacial components:

$$\vec{\beta} = \beta^i \vec{\partial}_i. \tag{3.20}$$

In short, in the $3+1$ formalism, each basis vector $\vec{\partial}_t$ is decomposed into one temporal part, $\vec{n}$, and a spatial part, $\vec{\beta}$ (Figure 3.2). The components of each of these vectors are related in the following way (which comes directly from Eq. (3.19)):

$$n^\alpha = \left(\frac{1}{N}, -\frac{\beta^1}{N}, -\frac{\beta^2}{N}, -\frac{\beta^3}{N} \right). \tag{3.21}$$

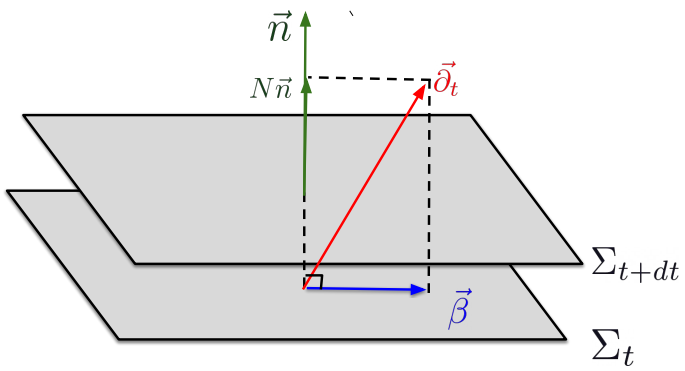

Figure 3.2: Decomposition of the basis vector $\vec{\partial}_t$.

Finally, the spacetime interval, $\mathrm{d}s$, in terms of components of the induced metric $\boldsymbol{\gamma}$, the shift vector and the lapse function is given by:

$$\mathrm{d}s = g_{\alpha\beta} = -N^2\mathrm{d}t^2 + \gamma_{ij}\left(dx^i + \beta^i\mathrm{d}t\right)\left(\mathrm{d}x^j + \beta^j\mathrm{d}t\right) \tag{3.22}$$

Intrinsic and extrinsic curvature

When one deals with a geometric structure that is embedded in a broader geometric structure, which is the case for the hypersurfaces Σ_t with respect to the manifold $\mathcal{M}$, it is important to distinguish between the notion of intrinsic and extrinsic curvatures. By intrinsic curvature we refer to the curvature that in the non-decomposed manifold $\mathcal{M}$ is measured by the Riemann curvature tensor (Equation 3.5). The intrinsic curvature of the hypersurfaces Σ_t can be contructed in an analogous way, by replacing the 4-dimensional metric $g_{\alpha\beta}$ by the induced metric γ_{ij}, and writing the corresponding connection coefficients for the 3-dimensional space [27]. Hereafter, we are going to identify these reduced 3-dimensional quantities with an upper left index 3 placed on the usual symbols (i.e, ${}^3R$ for the 3-dimensional Ricci scalar, ${}^3R_{ij}$ for the Riemann tensor, etc.)

The notion of extrinsic curvature emerges only when we consider a slice of an enveloping structure, and it measures how this slice is curved with respect to the full geometry. In our case the slices are, of course, the Σ_t hypersurfaces and the enveloping geometric structure is the spacetime $\mathcal{M}$. Borrowing the example from [27]:

> *A vector lying on the equator of the Earth and pointing toward the North Star, transported parallel to itself along a meridian to a point still on the Earth's surface, but* 1000 *km to the north, will no longer lie in the [same] 2-geometry of the surface of the Earth.*

By the same reasoning, as an interval of time $\mathrm{d}t$ passes, a vector lying in the hypersurface Σ_t will no longer be parallel to it, but will instead be part of a hypersurface $\Sigma_{t+\mathrm{d}t}$ and, therefore, the intrinsic curvature γ_{ij} defined on Σ_t is no longer applicable. Just like the Christoffel symbols allow to express the parallel transport of a vector on

a manifold $\mathcal{M}$, the exterior curvature tensor is introduced to account for the parallel transport across the hypersurfaces of $\mathcal{M}$.

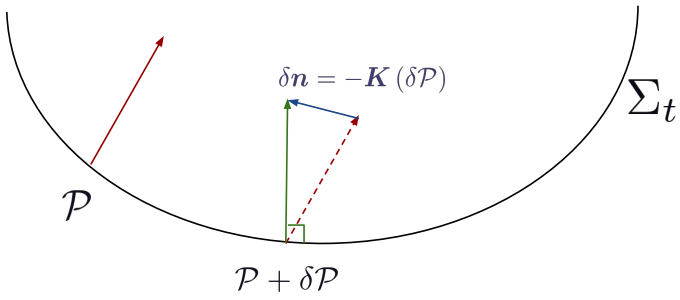

Figure 3.3: The notion of extrinsic curvature.

Heuristically [3], the extrinsic curvature tensor can be introduced by considering a vector lying at a point $\mathcal{P}$ of Σ_t which is parallel transported to the point $\mathcal{P} + \delta\mathcal{P}$ (Figure 3.3). The difference between the result of the parallel transport and the normal vector (of same magnitude) at the point $\mathcal{P} + \delta\mathcal{P}$ is vector $\delta\vec{n}$, which is parallel to Σ_t. The exterior curvature is the linear operator such that:

$$\delta\vec{n} = \boldsymbol{K}(\delta\mathcal{P}). \tag{3.23}$$

In more explicit way [21]

$$\forall(\vec{u},\vec{v}) \in \mathcal{T}_p(\Sigma_t) \times \mathcal{T}_p(\Sigma_t), \quad \boldsymbol{K}(\vec{u},\vec{v}) := -\vec{u}\cdot\nabla_{\vec{v}}\vec{n}, \tag{3.24}$$

where the operator $\nabla_{\vec{v}}$ stands for the directional derivative along $\vec{v}$. $\boldsymbol{K}$ is a symmetric tensor and its components with respect to the coordinates $\{x^i\}$ of Σ_t are given by

[3] A more rigorous treatment can be found in [27, 28]

$$K_{ij} = -\frac{1}{2N}\left(\frac{\partial \gamma_{ij}}{\partial t} - \mathcal{L}_{\vec{\beta}}\gamma_{ij}\right) = \frac{1}{2N}\left(-\frac{\partial \gamma_{ij}}{\partial t} + \beta^k \frac{\partial \gamma_{ij}}{\partial x^k} + \gamma_{kj}\frac{\partial \beta^k}{\partial x^i} + \gamma_{ik}\frac{\partial \beta^k}{\partial x^j}\right), \quad (3.25)$$

where $\mathcal{L}_{\vec{\beta}}\gamma_{ij}$ stands for the Lie derivative [4] of γ_{ij} along $\vec{\beta}$. The trace of $\boldsymbol{K}$ with respect to Σ_t is written as:

$$K := \gamma^{ij}K_{ij} = -\nabla_\mu n^\nu \quad (3.26)$$

Einstein's equations in the 3 + 1 formalism

In this formalism, the Einstein's equations are obtained from Equation (3.2) through a series of projections onto Σ_t and along $\vec{n}$ [21]:

$$\frac{\partial K_{ij}}{\partial t} - \mathcal{L}_{\vec{\beta}}K_{ij} = -D_iD_jN + N\{{}^3R_{ij} + KK_{ij} - 2K_{ik}K^k_j + 4\pi\left[(S-E)\,\gamma_{ij} - 2S_{ij}\right]\}, \quad (3.27)$$

$${}^3R + K^2 - K_{ij}K^{ij} = 16\pi E, \quad (3.28)$$

$$D_jK^j_i - D_iK = 8\pi p_i. \quad (3.29)$$

The quantities E, p_i and S_{ij} are the same quantities introduced in Equations (3.15) to (3.17). S is the trace of $\vec{S}$ with respect to the metric $\boldsymbol{\gamma}$: $S = \gamma^{ij}S_{ij}$. D_i are the components of the covariant derivative; with respect to the spatial coordinates $\{x^i\}$ of Σ_t, these can be written as:

$$D_iD_jN = \frac{\partial^2 N}{\mathrm{d}x^i\mathrm{d}x^j} - {}^3\Gamma^k_{ij}\frac{\partial}{\partial x^k}, \quad (3.30)$$

$$D_jK^j_i = \frac{\partial K^j_i}{\partial x^j} + {}^3\Gamma^j_{jk}K^k_i - {}^3\Gamma^k_{ji}K^j_k, \quad (3.31)$$

$$D_iK = \frac{\partial K}{\partial x^i}. \quad (3.32)$$

[4] The components of the Lie derivative of a field $\vec{v}$ along $\vec{u}$ in an arbitrary coordinate system can be written as $\mathcal{L}_{\vec{u}}v^\alpha = u^\mu \frac{\partial v^\alpha}{\partial x^\mu} - v^\mu \frac{\partial u^\alpha}{\partial x^\mu}$

3.3 Evolution Strategies

The $3+1$ Einstein's equations can be divided into two categories [29]:

- **Evolution equations**. This category corresponds to Eq. (3.27), and they govern the time evolution of the dynamical fields $\{\gamma_{ij}, K_{ij}\}$.
- **Energy and momentum constraints**. Given by Equations (3.28) and (3.29) respectively. These are constraints on the extrinsic curvature components K_{ij} and their spacial derivatives.

The structure of these equations resemble that of the Maxwell's equations in the non-covariant form:

$$\nabla \vec{E} = 4\pi\rho \tag{3.33}$$

$$\nabla \vec{H} = 0 \tag{3.34}$$

$$-\partial_t \vec{E} + \nabla \times \vec{H} = 4\pi \vec{j} \tag{3.35}$$

$$\partial_t \vec{H} + \nabla \times \vec{E} = 0. \tag{3.36}$$

This is not a mere coincidence. In fact, the same way the dynamical fields $\{\gamma_{ij}, K_{ij}\}$ emerge when one splits the manifold of general relativity into space and time, the fields $\{\vec{H}, \vec{E}\}$ are only defined when one splits the spacetime manifold into space and time. Otherwise one has to work with the more general electromagnetic 2-form $\boldsymbol{F}$ [30].

The similarities between the $3+1$ system and Maxwell's equations suggests that we borrow the equation-solving strategies from electromagnetism. More precisely, that we start by solving the constraint equations (which are first integrals of the evolution system) and, thus, obtaining four[5] of the six dynamical degrees of freedom (which correspond to the components of $\boldsymbol{K}$). The remaining degrees of freedom could then be obtained from Equation (3.27). This is known as the ***constrained evolution*** approach [29].

[5]Note that K is a symetric tensor.

The constrained evolution approach is analogous to electrostatics in the sense that the time evolution of the fields is not provided by the equations. Until recently, this approach was only used in 2D cases or when general relativity effects are considered lower corrections on Newtonian gravity [31]. In a simplified way, the constraint equations contain all of the dynamical degrees of freedom, except the ones related to gravitational radiation and with the coordinate gauge freedom [29]. Since there is no general way of algebraically singling out the dynamical degrees of freedom corresponding to gravitational radiation , a more general approach for solving the $3+1$ system is needed.

The predominant evolution approach for the $3+1$ system is known as the ***free evolution*** approach. This strategy consists in relying solely on Equation (3.27) to solve all the degrees of freedom, usually with either finite difference or finite element methods. The constraints (3.28) and (3.29) are solved only to get the initial data, but are not enforced during evolution (although they can be used as error indicators).

As for what concern us in this work, the calculation of the global properties of neutrons stars is a static problem [6] and therefore it is enough to solve the constraint equations (unlike the cases of mergers or Supernova collapses).

[6] That is why it was possible to perform our calculations on a simple laptop.

Chapter 4

Rotating Magnetized Stars

In order to apply our formalism to a real problem, we have to choose the coordinate system and, thus, the form of the metric tensor that we are going to work with. The convenience of a coordinate system is dependent upon the symmetries present in our system (in this case, in our spacetime manifold $\mathcal{M}$). Symmetries of the spacetime manifold are described in a coordinate-independent way by means of a symmetry group G acting on $\mathcal{M}$, and we require that the metric $\boldsymbol{g}$ remains invariant under such operation. The coordinate system that we are going to use is constructed on the assumption that that our spacetime $\mathcal{M}$, equiped with a metric $\boldsymbol{g}$, is both stationary and axisymmetric. A spacetime is said to be **stationary** if and only if there exists a group action on $\mathcal{M}$ such that:

1. the group is isomorphic to the group of unidimensional translations;
2. the orbits [1] are timelike curves in $\mathcal{M}$;
3. the metric is invariant under the group action, which equivalent to

$$\mathcal{L}_{\vec{\xi}}\boldsymbol{g} = 0, \tag{4.1}$$

[1] The orbit of a point $p \in \mathcal{M}$ is the set $\{g\,(p)\,, g \in G\} \subset \mathcal{M}$, i.e. the set of points that are connect to p by some group transformation g .

where $\mathcal{L}_{\vec{\xi}}\boldsymbol{g}$ stands for the Lie derivative of $\boldsymbol{g}$ along the vector field $\vec{\xi}$, which is the generator of G associated with some parameter t.

A spacetime is said to be **axisymmetric** if and only if there exists a group action on $\mathcal{M}$ such that:

1. the group G is isomorphic to SO(2), the group of rotations in the plane;
2. the set of points that remain invariant under G is a 2-dimensional surface of $\mathcal{M}$;
3. the metric is invariant under the group action, i.e.,

$$\mathcal{L}_{\vec{\chi}}\boldsymbol{g} = 0, \tag{4.2}$$

where $\vec{\chi}$ is the generator of G associated with some parameter ϕ. We will also consider our spacetime to be circular stationary which, if we choose spherical coordinates, allows one to write the spatial part of the metric tensor as a diagonal matrix [21].

4.1 Maximal slicing quasi-isotropic coordinates (MSQI)

In a stationary and circular axisymetric spacetime we may use adapted coordinates $\{t, r\theta, \phi\}$ such that the components of the metric tensor become:

$$g_{\alpha\beta}\mathrm{d}x^{\alpha}\mathrm{d}x^{\beta} = -N^2\mathrm{d}t^2 + A^2\left(\mathrm{d}r^2 + r^2\mathrm{d}\theta^2\right) + B^2r^2\sin^2\theta\left(\mathrm{d}\phi - N^{\phi}\mathrm{d}t\right)^2 \tag{4.3}$$

where N, A, B and N^{ϕ} are functions of (r, θ), sometimes represented by their logarithms:

$$\nu := \ln N; \quad \alpha := \ln A; \quad \beta := \ln B. \tag{4.4}$$

By comparing with Equation (3.22) one concludes that in this coordinate system the lapse function corresponds to the function $N(r, \theta)$ and that the shift vector has the following components:

$$\beta^i = \left(0, 0, -N^\phi\right). \tag{4.5}$$

We also identify the components of the induced metric $\boldsymbol{\gamma}$:

$$\gamma_{ij}\mathrm{d}x^i\mathrm{d}x^j = A^2\left(\mathrm{d}r^2 + r^2\mathrm{d}\theta^2\right) + B^2r^2\sin^2\theta\mathrm{d}\phi^2, \tag{4.6}$$

or simply

$$\gamma_{ij} = \mathbf{diag}\left(A^2, A^2r^2, B^2r^2\sin^2\theta\right). \tag{4.7}$$

From Equation (3.25) we can obtain the components of the extrinsic curvature tensor $\boldsymbol{K}$ of the hypersurfaces Σ_t:

$$K_{ij} = \frac{1}{2N}\left(-\underbrace{\frac{\partial\gamma_{ij}}{\partial t}}_{=0} - N^\phi\underbrace{\frac{\partial\gamma_{ij}}{\partial\phi}}_{=0} - \gamma_{\phi j}\frac{\partial N^\phi}{\partial x^i} - \gamma_{i\phi}\frac{\partial N^\phi}{\partial x^j}\right). \tag{4.8}$$

In the above equation the two derivatives vanished because of our symmetry considerations. The non-vanishing components of $\boldsymbol{K}$ are:

$$K_{r\phi} = K_{\phi r} = -\frac{B^2r^2\sin^2\theta}{2N}\frac{\partial N^\phi}{\partial r} \tag{4.9}$$

and

$$K_{\theta\phi} = K_{\phi\theta} = -\frac{B^2r^2\sin^2\theta}{2N}\frac{\partial N^\phi}{\partial\theta}. \tag{4.10}$$

The *maximal slicing* term stands for the fact that the trace of $\boldsymbol{K}$, as defined in Equation (3.26), vanishes identically [21]:

$$K = \gamma^{ij} K_{ij} = \frac{1}{A^2} \underbrace{K_{rr}}_{=0} + \frac{1}{A^2 r^2} \underbrace{K_{\theta\theta}}_{=0} + \frac{1}{B^2 r^2 \sin^2\theta} \underbrace{K_{\theta\theta}}_{=0}. \tag{4.11}$$

4.2 Einstein's equations in MSQI coordinates

The $3+1$ system of equations (3.27) to (3.29) can be written with MSQI coordinates by replacing the components of $\boldsymbol{K}$ and $\boldsymbol{\gamma}$ with their corresponding expressions in MSQI. By doing so, and after reorganizing the equations, one obtains [32]:

$$\Delta_3 \nu = 4\pi A^2 (E + S) + \frac{B^2 r^2 \sin^2\theta}{2N^2} \partial N^\phi \partial (\nu + \ln B) \tag{4.12}$$

$$\tilde{\Delta}_3 \left(N^\phi r \sin\theta \right) = -16\pi \frac{N A^2}{B^2} \frac{p_\phi}{r \sin\theta} + r \sin\theta \left(S_r^r + S_\theta^\theta \right) \tag{4.13}$$

$$\Delta_2 \left[(NB - 1) r \sin\theta \right] = 8\pi N A^2 B r \sin\theta \left(S_r^r + S_\theta^\theta \right) \tag{4.14}$$

$$\Delta_2 (\ln A + \nu) = 8\pi A^2 S_\phi^\phi + \frac{3B^2 r^2 \sin^2\theta}{4N^2} \partial N^\phi \partial N^\phi - \partial\nu\partial\nu. \tag{4.15}$$

In order to make the above equations less cumbersome, the following definitions were used:

$$\Delta_2 := \frac{\partial^2}{\partial r^2} + \frac{1}{r}\frac{\partial}{\partial r} + \frac{1}{r^2}\frac{\partial^2}{\partial\theta^2}, \tag{4.16}$$

$$\Delta_3 := \frac{\partial^2}{\partial r^2} + \frac{2}{r}\frac{\partial}{\partial r} + \frac{1}{r^2}\frac{\partial^2}{\partial\theta^2} + \frac{1}{r^2 \tan\theta}\frac{\partial}{\partial\theta} \tag{4.17}$$

$$\tilde{\Delta}_3 := \Delta_3 - \frac{1}{r^2 \sin^2\theta}. \tag{4.18}$$

Also, for any scalar fields u and v,

$$\partial u \partial v := \frac{\partial u}{\partial r}\frac{\partial v}{\partial r} + \frac{1}{r^2}\frac{\partial u}{\partial\theta}\frac{\partial v}{\partial\theta}. \tag{4.19}$$

Equations (4.12) to (4.14) form a system of elliptic partial differential equations and in order to be solved one has to impose the boundary conditions. Here we require that as $r \to \infty$, the metric tensor tends towards the Minkowski metric, which implies that:

$$\begin{cases} N\left(r,\theta\right) \\ A\left(r,\theta\right) \\ B\left(r,\theta\right) \\ N^{\phi}\left(r,\theta\right) \end{cases} \longrightarrow 1, \quad \text{as} \quad r \longrightarrow \infty. \tag{4.20}$$

4.3 Inclusion of rotation

As we have said in Chapter 2, the matter of stars is modeled as a perfect perfect fluid. Therefore, the description of a rotating star in general relativity consists in the description of a perfect fluid.

The circularity condition introduced in the discussion of the symmetries of our space-time implies that the fluid 4-velocity can be written as [21]:

$$\vec{u} = u^{i}\left(\vec{\xi} + \Omega\vec{\chi}\right), \tag{4.21}$$

where $\vec{\xi}$ and χ are the Lie vectors associated to the stationarity and axisymmetry, i.e,

$$\vec{\xi} = \vec{\partial}_{t}; \qquad \vec{\chi} = \vec{\partial}_{\phi}. \tag{4.22}$$

by expressing ξ in terms of the unit vector timelike vector $\vec{n}$ (the 4-velocity of the ZAMO), the fluid 4-velocity can be written as:

$$\vec{u} = \Gamma\left(\vec{n} + \vec{U}\right), \tag{4.23}$$

with

$$\Gamma = N u^t, \tag{4.24}$$

$$\vec{U} = \frac{1}{N}\left(\Omega - N^\phi\right)\vec{\chi}. \tag{4.25}$$

From the metric tensor in Equation (4.3), we conclude that $\vec{\chi}\cdot\vec{\chi} = B^2 r^2 \sin^2\theta$. Since $\vec{n}$ is an unit timelike vector, then $\vec{n}\cdot\vec{n} = -1$ and $\vec{n}\cdot\vec{U} = 0$. If we now define

$$U := \frac{B}{N}\left(\Omega - N^\phi\right) r\sin\theta \quad \Longrightarrow \quad \vec{U}\cdot\vec{U} = U^2, \tag{4.26}$$

the normalization[2] $\vec{u}\cdot\vec{u} = -1$ implies that

$$\Gamma = \left(1 - U^2\right)^{-1/2}. \tag{4.27}$$

The remaining task consists in writing the quantities that act as source terms for the Einstein's equations, i.e, E, p_ϕ, S^r_r, S^θ_θ and S^ϕ_ϕ. This can be achieved by substituting in Equations (3.15) to (3.17), the 4-velocity $\vec{u}$ expressed in terms of Γ and the components of $\vec{U}$. As result one obtains:

$$E = \Gamma^2(\epsilon + p) - p, \tag{4.28}$$

$$p_\phi = B(E + p)\,U r\sin\theta, \tag{4.29}$$

$$S^r_r = S^\theta_\theta = p, \tag{4.30}$$

$$S^\phi_\phi = p + (E + p)\,U^2, \tag{4.31}$$

$$S = 3p + (E + p)\,U^2, \tag{4.32}$$

where we also used the general form for a perfect fluid energy-momentum tensor [20]:

$$T_{\mu\nu} = (\epsilon + p)\,u_\mu u_\nu + p g_{\mu\nu}. \tag{4.33}$$

[2] This consequence of the unit choice.

Fluid conservation laws

The equations of motion for the fluid are the energy-momentum conservation law

$$\nabla^{\mu} T_{\mu\nu} = 0, \tag{4.34}$$

and the baryon number conservation law:

$$\nabla_{\mu} \left(n_b \, u^{\mu} \right) = 0. \tag{4.35}$$

From those equations we can obtain the general relativity equivalent of Bernoulli's equations which, for the rigid rotation case, has the following form:

$$H + \nu - \ln \Gamma = \text{const.}\,, \tag{4.36}$$

where H is the logarithm of the enthalpy per baryon, i.e,

$$H := \ln \left(\frac{h}{m_b} \right). \tag{4.37}$$

Numerical procedure

We are now in condition to sketch the numerical procedure[3] used in LORENE in the calculations of rotating stars. Inside the LORENE library, the code that calculates the global properties of non-magnetized rotating stars is under the name of *Nrotstar*. A review on the topic as well a "side by side" comparison of the different methods for rotating stars' calculations can be found in [33].

The inputs of the code are the following:

[3]The title "numerical procedure" is a bit misleading , since the actual code is going to be much more complex than what we present here (we do not even dwelve on the numerical methods for the partial differential equations). An accessible discussion on the actual implementation of the 3+1 formalism can be found in [29].

- Equation of state in the form $\epsilon = \epsilon(H)$ and $p = p(H)$;
- central value H_c of the log-enthalphy H. This also equivalent to fixing the total baryonic mass of the star;
- the value of the angular velocity , Ω.

The calculations are then performed in the following way [21]:

1. The quantities N, N^{ϕ}, A and B receive initial guesses; U is set to zero, and ϵ and p are calculated from the EOS.
2. The Einstein's equations sources terms are calculated from U, Γ, ϵ and p.
3. Using the initial guesses, the Einsteins equations are solved in order to obtain new values for N, N^{ϕ}, A and B.
4. U and Γ are calculated with the new values of N, N^{ϕ}, A and B.
5. H is calculated from Equation (4.36), with H_c as the constant.
6. Go to step 2.

4.4 Inclusion of magnetic field

The self consistent method for calculation of magnetized rotating stars that we discuss here was introduced in [34]. In a nutshell, the inclusion of magnetic field contribution is achieved by adding the electromagnetic field tensor to the energy-momentum tensor (previously described only by the perfect fluid energy-momentum tensor). By doing so, in addition to Einstein's equations one has to solve to solve Maxwell's equations too.

We will consider the same metric tensor given by Equation (4.3) and we will also work with the MSQI coordinate system. The most general form for the electric 4-current that satisfies our symmetry consideration has the following components: $j^{\alpha} = \left(j^{t}, 0, 0, j^{\phi}\right)$.

The corresponding electromagnetic tensor $\boldsymbol{F}$ is obtained from a potential 1-form A with components $A_\alpha = (A_t, 0, 0, A_\phi)$:

$$F_{\alpha\beta} = A_{\beta,\alpha} - A_{\alpha,\beta}. \tag{4.38}$$

From the components of $\boldsymbol{F}$ one obtains the components of the electric, $\boldsymbol{E}$, and magnetic, $\boldsymbol{B}$, fields. In respect to the ZAMO, these components read:

$$\begin{aligned} E_\alpha &= F_{\alpha\beta} n^\beta \\ &= \left(0, \frac{1}{N}\left[\frac{\partial A_t}{\partial r} + N^\phi \frac{\partial A_\phi}{\partial r}\right], \frac{1}{N}\left[\frac{\partial A_t}{\partial \theta} + N^\phi \frac{\partial A_\phi}{\partial \theta}\right], 0\right) \end{aligned} \tag{4.39}$$

and

$$\begin{aligned} B_\alpha &= -\frac{1}{2}\epsilon_{\alpha\beta\mu\nu} n^\beta F^{\mu\nu} \\ &= \left(0, \frac{1}{A^2 B r^2 \sin\theta}\frac{\partial A_\phi}{\partial \theta}, -\frac{1}{A^2 B \sin\theta}\frac{\partial A_\phi}{\partial r}, 0\right), \end{aligned} \tag{4.40}$$

where $\epsilon_{\alpha\beta\mu\nu}$ is the Levi-Civita tensor associated with the metric $\boldsymbol{g}$.

The dynamics of the electromagnetic field is governed by Maxwell's equations. The homogeneous equation is satisfied automatically from the form of $\boldsymbol{F}$ (Equation 4.38). The remaining equations, $F^{\alpha\beta}_{;\beta} = \mu_0 j^\alpha$, become:

$$\begin{aligned} \Delta_3 A_t = &-\mu_0 \frac{A^4}{B^2}\left(g_{tt} j^t + g_{t\phi} j^\phi\right) - \frac{A^4 B^2}{N^2} N^\phi r^2 \sin^2\theta \\ &\partial A_t \partial N^\phi - \left(1 + \frac{A^4 B^2}{N^2} r^2 \sin^2\theta \left(N^\phi\right)^2\right) \\ &\partial A_\phi \partial N^\phi - \left(\partial A_t + 2 N^\phi \partial A_\phi\right) \partial\left(2\alpha + \beta - \nu\right) \\ &- 2\frac{N^\phi}{r}\left(\frac{\partial A_\phi}{\partial r} + \frac{1}{r\tan\theta}\frac{\partial A_\phi}{\partial \theta}\right), \end{aligned} \tag{4.41}$$

and

$$\begin{aligned}\tilde{\Delta}_3\tilde{A}^{\phi} = &-\mu_0 A^8\left(j^{\phi}-N^{\phi}j^{t}\right)r\sin\theta+\frac{A^4B^2}{N^2}r\sin\theta\partial N^{\phi}\left(\partial A_t+N^{\phi}\partial A_{\phi}\right)\\&+\frac{1}{rsin\theta}\partial A_{\phi}\partial\left(2\alpha+\beta-\nu\right),\end{aligned} \tag{4.42}$$

where

$$\tilde{A}^{\phi} := \frac{A_{\phi}}{r\sin\theta}, \tag{4.43}$$

and we have used the definitions introduced in Equations (4.16) – (4.19).

4.4.1 Lorentz force and condition for stationary motion

Taking into account the electromagnetic field on the fluid, Bernoulli's equation becomes:

$$H\left(r,\theta\right)+\nu\left(r,\theta\right)-\ln\Gamma\left(r,\theta\right)+M\left(r,\theta\right)=\text{const.} \tag{4.44}$$

The function M is called the magnetic potential and is a function of A_{ϕ} only and can be written as [32]

$$M\left(r,\theta\right)=M\left(A_{\phi}\left(r,\theta\right)\right)=-\int_0^{A_{\phi}(r,\theta)}f\left(x\right)\mathrm{d}x, \tag{4.45}$$

where f is an arbitrary function that we call the current function. The gradient of the magnetic potential, M, is proportional to the Lorenz force [35]:

$$\boldsymbol{F}_L\sim\nabla M\left(r,\theta\right) \tag{4.46}$$

4.4.2 Perfect conductor relation

If we assume that the fluid has infinite conductivity, then the following relation holds [36]:

$$\frac{\partial A_t}{\partial x^i}=-\Omega\frac{\partial A_{\phi}}{\partial x^i}, \tag{4.47}$$

where Ω is the rotation frequency. It can be shown that a stationary configuration with a magnetic field is necessarily rigidly rotating, i.e, $\Omega = \text{const.}$ [32], which implies that

$$A_t = -\Omega A_\phi + C, \tag{4.48}$$

where C is a constant that determines the total electric charge of the star.

Numerical procedure

Inside the LORENE library, the code that calculates the global properties of rotating magnetized stars is under the name of *Mag_eos_star*. In addition to the inputs discussed in the non-magnetized case, one has to specify the following quantities:

- Total electric charge, Q. In our calculations we have required that $Q = 0$.
- Choose a current function , f. In LORENE f is constant value function, i.e, $f = f_0$, where f_0 is called the current function amplitude.

The iterative procedure is also similar to the non-magnetized case, except that now one has to calculate the fields A_t and A_ϕ (similarly to N, N^ϕ, A and B):

- In the first step A_ϕ is set to zero and A_t is calculated from Equation (4.48). The components of $\vec{j}$ are calculated using Maxwell's equations
- With the components of $\vec{j}$ obtained in the previous steps, we obtain new values for A_ϕ and A_t.

4.5 Global properties of stars

In this section we present the definitions of some general relativity quantities that are relevant for the understanding of our results.

Baryon mass

The baryon mass of the star is defined as:

$$M_b := m_b \mathcal{N}, \tag{4.49}$$

where m_b is the mean baryon mass ($m_b \approx 1.66 \times 10^{-27}$ Kg) and $\mathcal{N}$ is the total baryon number.

If n_b represents the baryon number density in the fluid frame and $\vec{u}$ is the fluid 4-velocity, then the baryon 4-current can be expressed as:

$$\vec{j_b} = n_b \vec{u}. \tag{4.50}$$

The baryon number density n_b is related to the EOS and to the log-enthalpy H in the following way:

$$n_b = \frac{\epsilon + p}{m_b} \exp\left(-H\right). \tag{4.51}$$

The conservation law of the baryon 4-current, $\vec{j_b}$ can be expressed as:

$$\nabla_\mu j_b^\mu = 0. \tag{4.52}$$

By applying the divergence theorem one obtains:

$$\mathcal{N} := -\int_{\Sigma_t} \vec{j_b} \cdot \vec{n} \sqrt{\gamma} \mathrm{d}x^i \mathrm{d}x^2 \mathrm{d}x^3, \tag{4.53}$$

where $\sqrt{\gamma}$ is the square root of the determinant of the tensor $\boldsymbol{\gamma}$ in MSQI coordinates, i.e, $\sqrt{\gamma} = A^2 B r^2 \sin\theta$. This definition of $\mathcal{N}$ is independent on the slicing $\{\Sigma_t\}$ of the spacetime.

Mass

The *observable* mass of a star is what we call as **gravitational mass**, M. This mass is related to the baryon mass through the following relation

$$M = M_b + E_{bind}, \tag{4.54}$$

Where E_{bind} is called the **binding energy** and is the amount of energy required to hold the system of $\mathbb{N}$ particles together through gravity. The way we define M depends on the properties of the system. For any asymptotically flat spacelike hypersurface Σ_t one can use the **ADM mass** introduced by Arnowitt, Deser and Misner in [37]. In MSQI coordinates this mass can be written as:

$$M_{ADM} = -\frac{1}{16\pi} \lim_{\mathcal{S}} \oint_{\mathcal{S}} \left[\frac{\partial}{\partial r} \left(A^2 + B^2 \right) + \frac{B^2 - A^2}{r} \right] r^2 \sin\theta \mathrm{d}\theta \mathrm{d}\phi. \tag{4.55}$$

Coordinate radius and circumferential radius

In the discussion of our results we are going to use what is called as **coordinate radius** of the star. This quantity is simply the coordinate r that corresponds to the surface of the star, defined as the point at which the value of the enthalpy reaches zero. The radius defined this way is coordinate dependent. This is not a problem in our discussion as we compare results measured with the same coordinates. A coordinate-independent definition of the star radius is the **circumferential radius**. This quantity can be understood as the radius associated with a circumference of length l:

$$R_{circ} := \frac{l}{2\pi}. \tag{4.56}$$

In MSQI coordinates, this quantity can be written in terms of the coordinate radius, R, in the following way:

$$R_{circ} = B\left(R_{eq}, \pi/2\right) R_{eq}. \tag{4.57}$$

Chapter 5

Results

The results[1] that we present in this section were obtained through a set of numerical simulations performed with LORENE library, whose mathematical building blocks were already discussed in Chapters 3 and 4. In order to use LORENE's output to calculate the quantities that interest us, we have written a set of auxiliary python routines, which we organized in the form of a GitHub repository [38]. These Python routines also served as a more practical interface for LORENE.

As discussed in Chapter 2, by calculating the dynamical spinodal of magnetized nuclear matter we conclude that between the core and the inner crust there is a region where stable and unstable matter interchange (Fig. 2.2), identified by the densities ρ_1 and ρ_2. We shall denote the radii that correspond to each of these densities as R_1 and R_2, respectively (cf. Figure 5.1). In this notation the thickness of the extended crust is defined as ($\Delta R_t = R_1 - R_2$), whilst the total size of the crust is given by the difference $\Delta R_2 = R - R_2$ (with R being the coordinate radius of the star). The difference $\Delta R_1 = R - R_1$ corresponds to the size of the crust without the extended region.

[1] The raw data can be found in `https://github.com/ivoabs/IS_MSThesis_data`

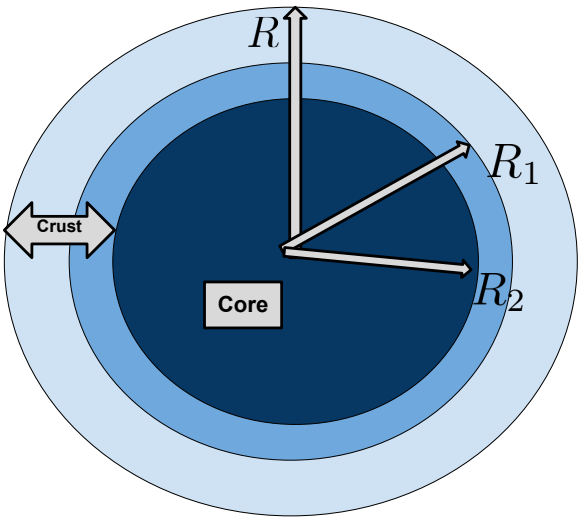

Figure 5.1: Definition of the quantities R_1 and R_2 (not in scale).

Table 5.1: Crust-core transition densities for NL3$\omega\rho$ with $L = 55$ MeV. Here $\rho_1 = \rho(R_1)$ and $\rho_2 = \rho(R_2)$.

B (4.41×10^{15} G)	ρ_1 (fm $^{-3}$)	ρ_2 (fm $^{-3}$)
0	0.084	———
1	0.0837	0.1044
5	0.08116	0.10996
10	0.0827	0.1096

Table 5.2: Crust-core transition densities for NL3$\omega\rho$ with $L = 88$ MeV. Here $\rho_1 = \rho(R_1)$ and $\rho_2 = \rho(R_2)$.

B (4.41×10^{15} G)	ρ_1 (fm $^{-3}$)	ρ_2 (fm $^{-3}$)
0	0.063	———
1	0.05951	0.12977
5	0.05485	0.12955
10	0.04874	0.13069

In a previous work [39], the authors have also studied the structure of neutron stars under the effect of strong magnetic fields, where they have used three EOS with different compositions. Here we restrict our study to two models of the NL3$\omega\rho$ family: one with the symmetry energy slope $L = 55$ MeV and other with $L = 88$ MeV. These models are able to generate two-solar-mass stars. The properties for symmetric nuclear matter at saturation density for these two models are shown in Table 5.3.

Table 5.3: Properties of the two models of the NL3$\omega\rho$ family for symmetric nuclear matter at saturation density ($\rho_0 = 0.148$ fm^{-3}).

L (MeV)	Binding energy, B/A (MeV)	Incompressibility, K (MeV)	Symmetry energy, E_{sym} (MeV)
55	-16.24	270	31.47
88	-16.24	270	34.88

5.1 Magnetic field effects on the crust

In this section we focus on the effects of strong magnetic fields on the geometry of the star and, particularly, of the inner crust. This is achieved by evaluating how the quantities R_1, R_2 and R vary with the magnetic field. As explained in Chapter 4, the configuration of the magnetic field on the star, as well as its magnitude, can be imposed by choosing the appropriate current function. In LORENE, such a function is a constant

function and it gives rise to a poloidal magnetic field. The magnitude is determined by the value of this constant, which we will, thereafter, designate by current function amplitude or, simply, CFA.

Since we could only fix the magnetic field by choosing the CFA value, we first needed to obtain a correspondence between the imposed CFA value and the actual value of the magnetic field measured inside the star. This was achieved by plotting the value of the surface field (the radial coordinate measured at the pole) as function of CFA. The CFA value that gives the desired value magnetic field amplitude could then be found by means of a numerical interpolation.

In Figure 5.2 we show – for three stellar mass values and for the two models considered – how the crust size varies with the magnetic field. We immediately note that the bigger the mass is, the smaller is the crust size. This is not a particular feature of the crust, but of the star as a whole: for the same family of stars, the high-mass stars are smaller than lower-mass stars [8]. Gravitation attraction is stronger for high masses and, therefore, they become more "shrunk". We can see that for $B_S = 0$ the results for the two models do not differ much from each other in comparison with the case where $B_S \neq 0$. However a small difference does exist as discussed in [40], where it was shown that the larger the slope L, the smaller the transition density, ρ_2, to the core. This, in turn, reflects itself on the thickness of the crust: a thinner crust corresponds to a larger L. A much greater difference is verified for $B_S \neq 0$. This is because the value ρ_2 (from which we define the crust size) depends on the proton fraction value which, in turn, depends on the value of the slope of symmetry energy [41]. Therefore, even though both models might have some resemblances at $B = 0$, they will respond differently with the inclusion of the magnetic field.

Still looking at figure 5.2 and taking as reference the values obtained with $M_b = 1.5\,\mathrm{M}_\odot$, we estimate that for the model with $L = 55$ MeV there is a variation of 13% from $B_S = 0$ to $B_S = 4.4 \cdot 10^{15}$ G. From $B_S = 4.4 \cdot 10^{15}$– $4.4 \cdot 10^{16}$ G the variation is roughly 2%. The model with $L = 88$ MeV shows a much bigger sensitivity on the increase of the magnetic field: from $B_S = 0$ – $4.4 \cdot 10^{15}$G there is a variation of 88%, whilst from

$B_S = 4.4 \cdot 10^{15}$ – $4.4 \cdot 10^{16}$G the variation is of approximately 1.5%. The reason lies in the fact that for densities below saturation density, the fraction of protons is smaller for larger values of L and, therefore, more sensitive to a given value of magnetic field (cf. Figure 5.3).

Although the overall trend is an increase of the crust size with the magnetic field, it is important to note that this behavior is not monotonic. In fact, from $B_S = 4.4 \cdot 10^{15}$ – $4.4 \cdot 10^{16}$G the variation on the $L = 88$ MeV model is negative.This is in agreement with the way the densities ρ_1 and ρ_2 vary with the field (Tables 5.1 – 5.2) and, as noted in [2], this is due to the discrete feature of the Landau levels (from which we calculate such densities). This effect is also present in Figure 5.4, where we show the size of the stable matter zone. Here the overall trend is that the size of the stable matter is reduced as the magnetic field increases, but this behavior is also not monotonic. Besides, this effect is much more monotonical for the $L = 88$ MeV model, due to the smaller proton fraction.

Figure 5.5 puts even more in evidence the fact that the effects introduced by the magnetic field are dependent on the symmetry energy slope, L. For the model with $L = 88$ MeV, we note that the extended crust occupies about one third of the total crust zone. This is more evident in Figure 5.8, where we plot the profile of each star that we have considered and, in each of them, we identify the extended zone. The main effect is an increase of the equatorial radius with respect to the polar one.

In Figure 5.6 we have used the results obtained with the stronger magnetic field value ($B = 4.41 \cdot 10^{16}$ G at the surface) to show how the crust varies along the polar angle θ. We normalized the curves with the values obtained with $B = 0$: for both R_1 and R_2, we divide the values obtained with $B_S = 4.41 \cdot 10^{16}$ G by the corresponding values (i.e. same mass and same L) obtained at $B = 0$. Since the values ρ_1 and ρ_2 do not have any spatial dependency, the results that we observe here are only consequence of the overall deformation of the star induced by the magnetic field. In fact, the way the crust is deformed is quite similar to the deformation of the radius (i.e., coordinate radius) of the star itself, as shown in Figure 5.7.

From figure 5.6 it is clear that the effect of the magnetic field is much stronger in the $L = 88$ MeV model: the difference between the equatorial and polar radii is larger; the extended crust extends much more into the interior of the star.

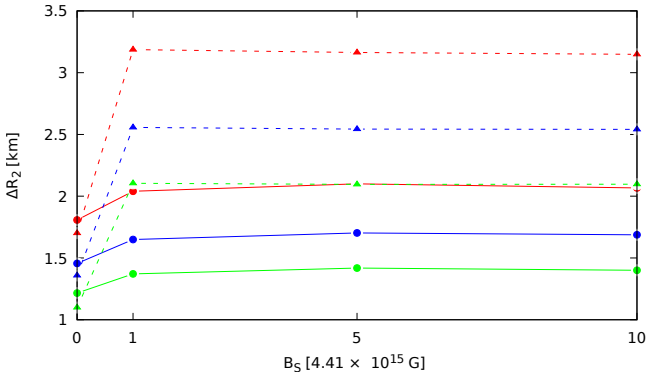

Figure 5.2: Total size of the crust as function of the magnetic field. Full lines correspond to the model with $L = 55$ MeV, whilst dashed lines come from the $L = 88$ MeV model. The colours red, blue and green correspond to baryon masses $1.2M_\odot$,$1.5M_\odot$ and $1.8M_\odot$, respectively.

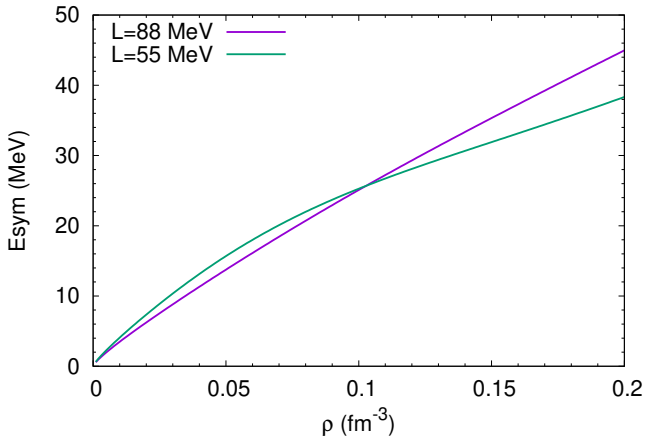

Figure 5.3: Symmetry energy as function of density, ρ, for the models with $L = 55$ MeV and $L = 88$ MeV.

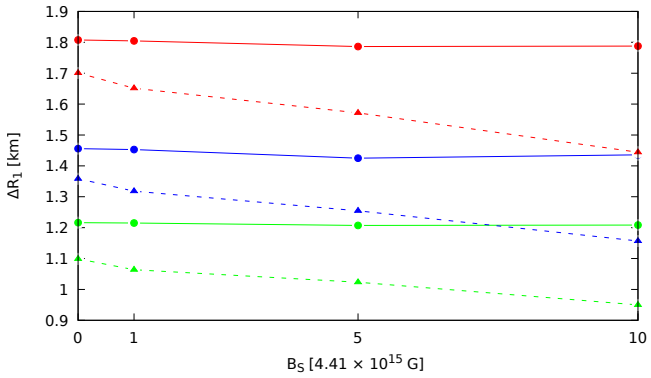

Figure 5.4: Size of the crust without the extended zone, plotted as function of the magnetic field. Full lines correspond to the model with $L = 55$ MeV, whilst dashed lines come from the $L = 88$ MeV model. The colours red, blue and green correspond to baryon masses $1.2M_\odot$,$1.5M_\odot$ and $1.8M_\odot$, respectively.

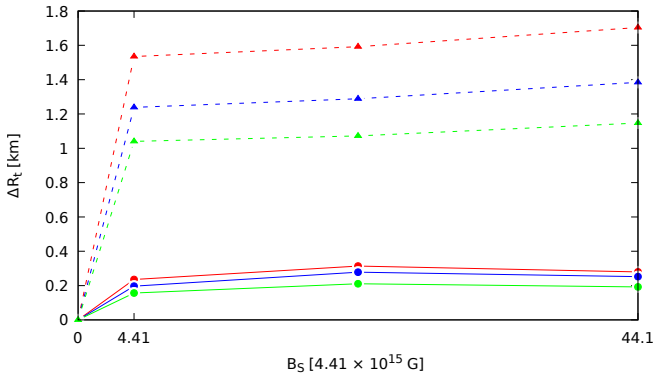

Figure 5.5: Thickness of the extended crust as function of the magnetic field. Full lines correspond to the model with $L = 55$ MeV, whilst dashed lines come from the $L = 88$ MeV model. The colours red, blue and green correspond to baryon masses $1.2M_\odot$,$1.5M_\odot$ and $1.8M_\odot$, respectively.

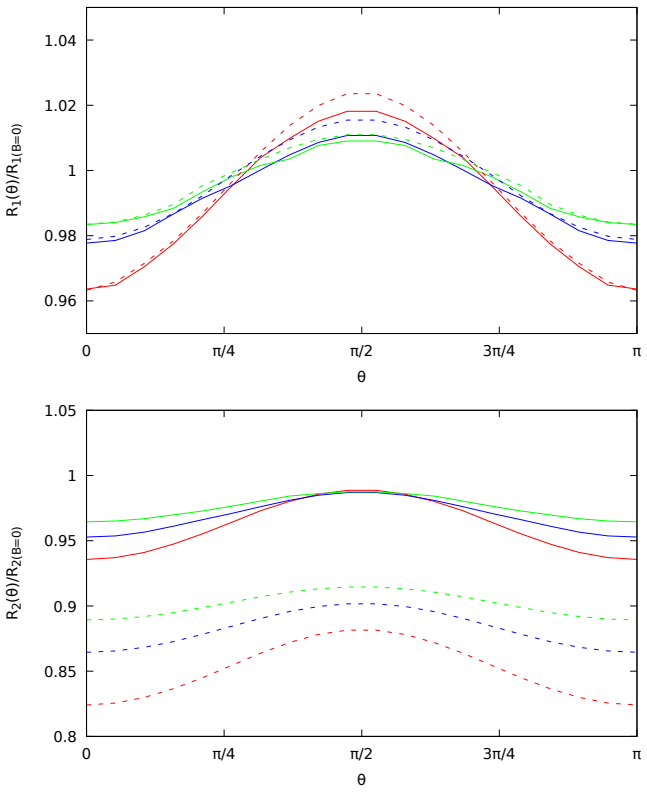

Figure 5.6: Normalised R_1 and R_2. In the top panel, each line represents, for a particular model and mass value, how R_1 varies with θ. In each case, the value of $R_1(\theta)$ obtained with $B_S = 4.4 \cdot 10^{16}$ G is divided by the corresponding value when the magnetic field is turned off. In the bottom panel we do the same for R_2 (notice that $R_2\,(B = 0) = R_1\,(B = 0)$). As before, Full lines correspond to the $L = 55$ MeV, whilst dashed lines come from the $L = 88$ MeV model. The colours red, blue and green correspond to baryon masses $1.2\mathrm{M}_\odot$,$1.5\mathrm{M}_\odot$ and $1.8\mathrm{M}_\odot$, respectively.

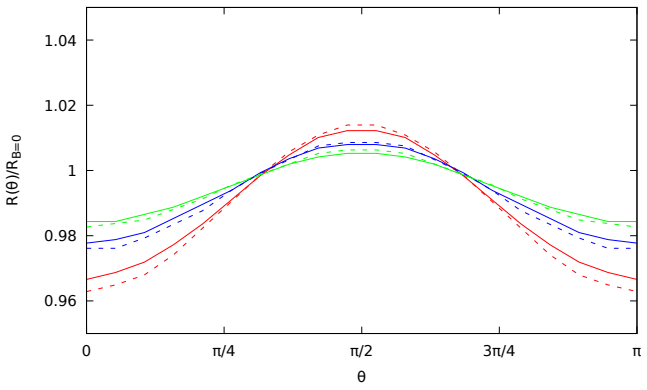

Figure 5.7: Here we show how R, the coordinate radius, varies with θ. In each case, the value of $R(\theta)$ is divided by the corresponding value when the magnetic field is turned off. Full lines correspond to the model with $L = 55$ MeV, whilst dashed lines come from $L = 88$ MeV. The colours red, blue and green correspond to baryon masses $1.2M_\odot$,$1.5M_\odot$ and $1.8M_\odot$, respectively

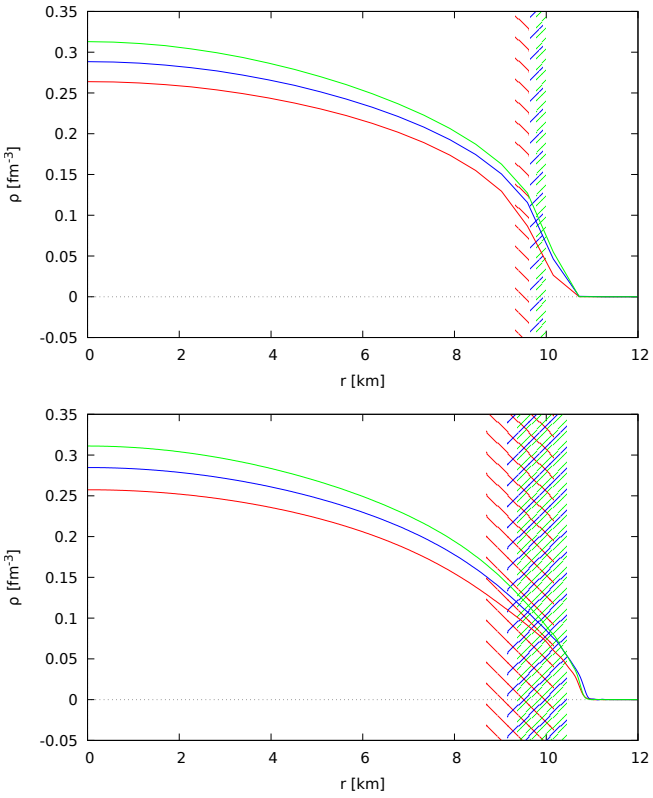

Figure 5.8: Baryon density as function of the radial coordinate. The top panel corresponds to $L = 55$ MeV whilst the bottom one corresponds to $L = 88$ MeV. The colours red, blue and green correspond to baryon masses $1.2M_{\odot}$,$1.5M_{\odot}$ and $1.8M_{\odot}$, respectively. The vertical bands correspond to the instability zones of the crust-core transition.

5.2 Magnetic potential

In this section we analyze the magnetic potential and how it relates to the instability region of the crust discussed previously. We are interested in this quantity because, as explained in Chapter 4, the gradient of the magnetic potential is proportional to the Lorenz force. All of the results presented in this section were obtained by setting the CFA to the one that gives a surface field of 4.4×10^{16} G.

In Figure 5.9 we show how the profile of the magnetic potential, M, varies along the star for the three masses and each model considered. We see that the magnitude of M

is larger inside the lighter stars. On the other hand, we also see that the magnitude of M is larger for the $L = 55$ MeV model. This might be because the core is larger for the $L = 55$ MeV model.

In Figures 5.10 to 5.12 we only consider the magnetic potential along the equatorial plane ($\theta = \pi/2$) and we identify the extended region, as well as the onset points of the different pasta phases of the crust matter. By doing so we want to ascertain if the points at which the Lorenz force changes sign, i.e., at which the function $M(r, \theta)$ has a minimum, and the points where the Lorenz force is maximum, i.e., the derivative of M has maximum, ever fall into the extended crust region. Figures 5.10 – 5.12 tell us that is not the case for the minimum of M for both models considered. One could wonder if the fact that the minimum of M does not fall into the extended crust (or the interior of the inner crust) is only a feature of the plane in which we are evaluating the function (since the position of the minimum depends on θ) . We have written a simple routine (which can be found on the same repository [38]) to verify if that is the case and the answer was negative: for the models and masses that we have considered, the minimum of the magnetic potential always falls into the core of the star. The fact that the minimum of M is located in the core is consistent with the results obtained in [2]. But we were expecting that by including the effects of the magnetic field on the spinodal, and thus having a more accurate description of the size of the crust, we would find out that this point was in fact part of the inner crust.

But, on the other hand, one of the maximums of the Lorenz force does fall inside the extended crust whilst the other fall well inside the crust, as can be seen in Figures 5.13 to 5.15. We may assume that a maximum of the Lorenz force inside the non-homogeneous region of the star may cause the matter to fract or break. On the right panels of Figures 5.10 – 5.15 we identify the location of the pasta phases. In the case of the $L = 88$ MeV model, no inner crust configurations besides droplets exist. However for the $L = 55$ MeV the maximum of the Lorenz force occurs near the region of rod like configurations, which may be easier to deform.

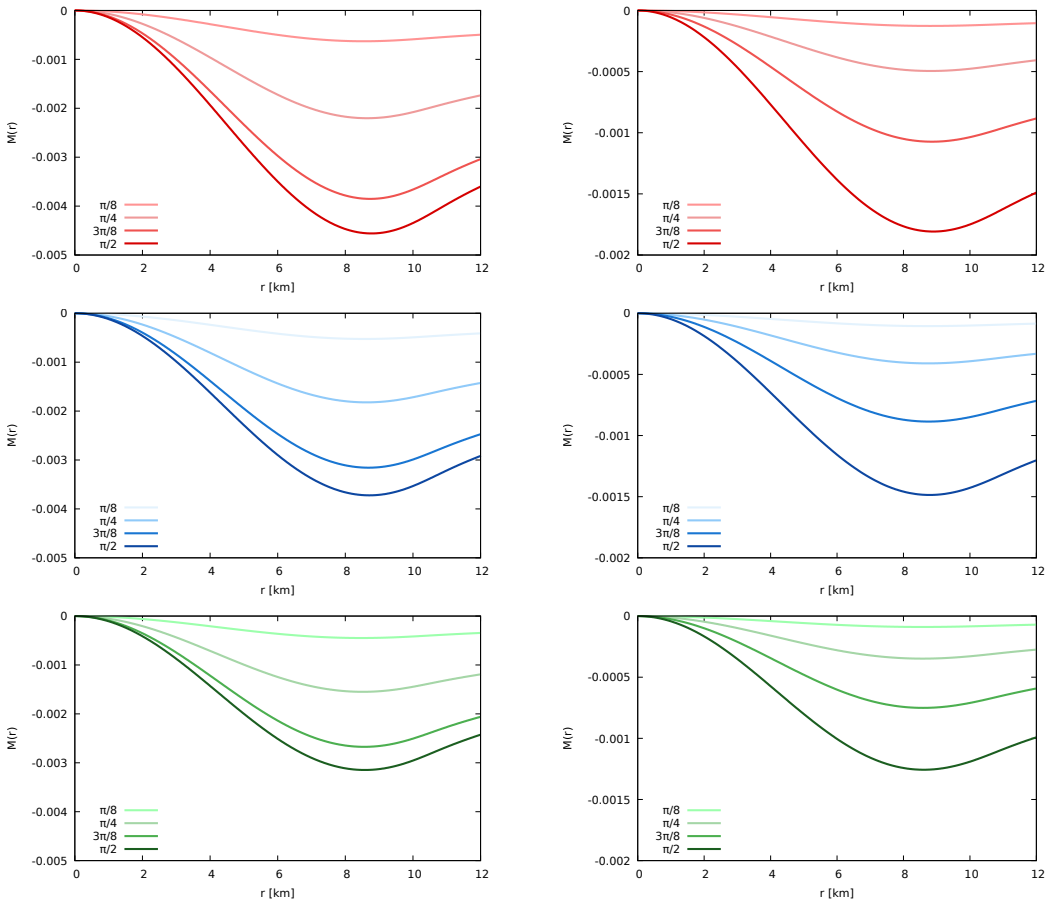

(a) $L = 55$ MeV (b) $L = 88$ MeV

Figure 5.9: Magnetic potential, M, as function of the radial coordinate. Results obtained with $B_S = 4.4 \times 10^{16}$ G. On the left panel we present the results obtained with $L = 55$ MeV and on the right the ones corresponding to $L = 88$ MeV. The colours red, blue and green correspond to baryon masses $1.2M_\odot$,$1.5M_\odot$ and $1.8M_\odot$, respectively. Notice the difference in the scale from the left to the right panels.

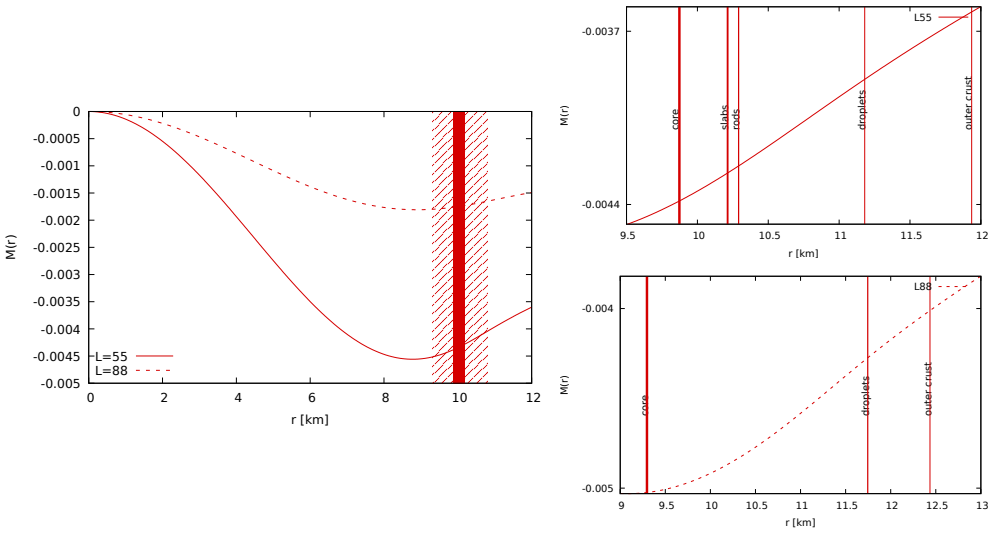

Figure 5.10: Magnetic potential, M, as function of the radial coordinate for a $M_b = 1.2\mathrm{M}_\odot$ star with $B_S = 4.4 \times 10^{16}$ G. Full lines correspond to the model with $L = 55$ MeV, whilst dashed lines come from the $L = 88$ MeV model. In the plots on the right we have amplified the region inside the crust and identified the location of the transition between the different pasta phases.

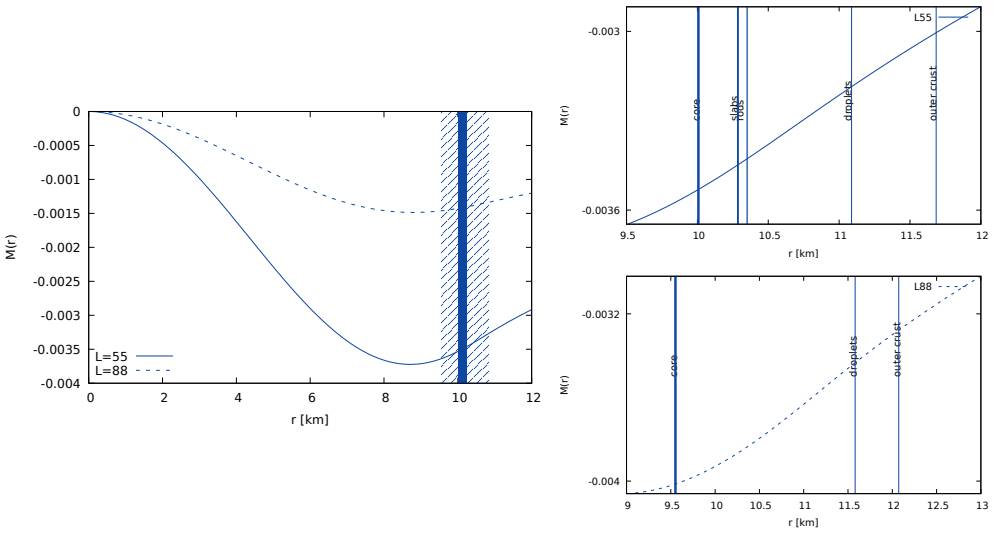

Figure 5.11: Magnetic potential, M, as function of the radial coordinate for a $M_b = 1.5\mathrm{M}_\odot$ star with $B_S = 4.4 \times 10^{16}$ G. Full lines correspond to the model with $L = 55$ MeV, whilst dashed lines come from the $L = 88$ MeV model. In the plots on the right we have amplified the region inside the crust and identified the location of the transition between the different pasta phases.

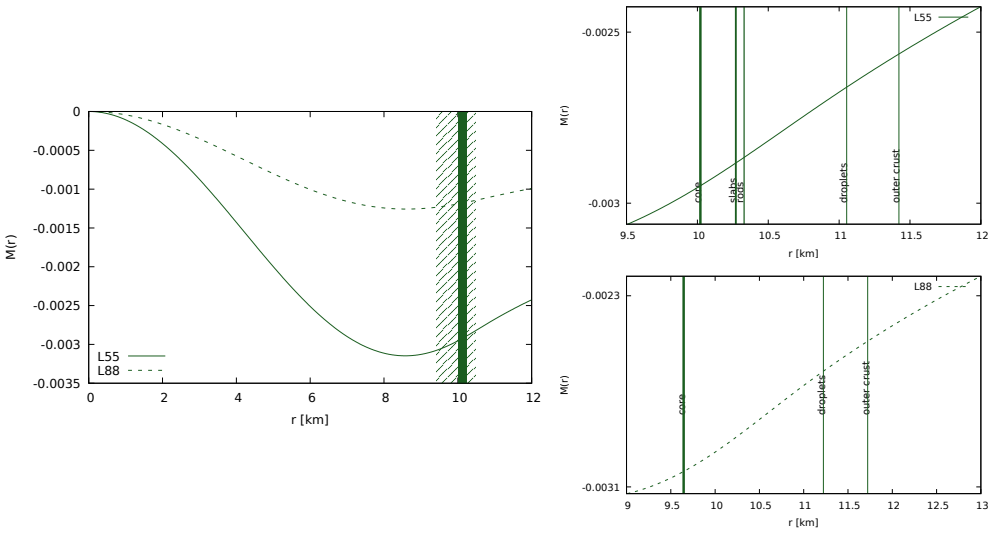

Figure 5.12: Magnetic potential, M, as function of the radial coordinate for a $M_b = 1.8\mathrm{M}_\odot$ star with $B_S = 4.4 \times 10^{16}$ G. Full lines correspond to the model with $L = 55$ MeV, whilst dashed lines come from the $L = 88$ MeV model. In the plots on the right we have amplified the region inside the crust and identified the location of the transition between the different pasta phases.

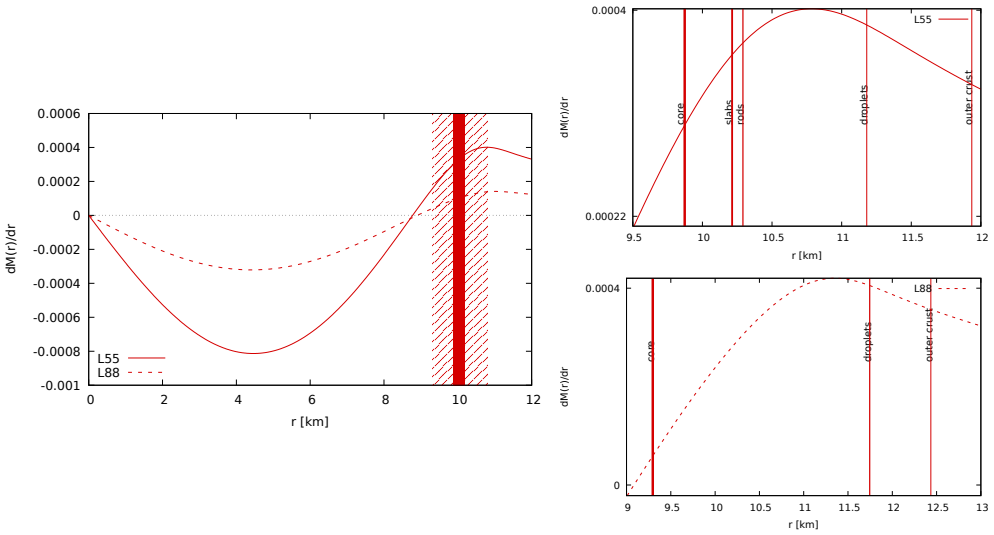

Figure 5.13: Derivative of the magnetic potential, as function of the radial coordinate for a $M_b = 1.2\mathrm{M}_\odot$ star with $B_S = 4.4 \times 10^{16}$ G. Full lines correspond to the model with $L = 55$ MeV, whilst dashed lines come from the $L = 88$ MeV model. In the plots on the right we have amplified the region inside the crust and identified the location of the transition between the different pasta phases.

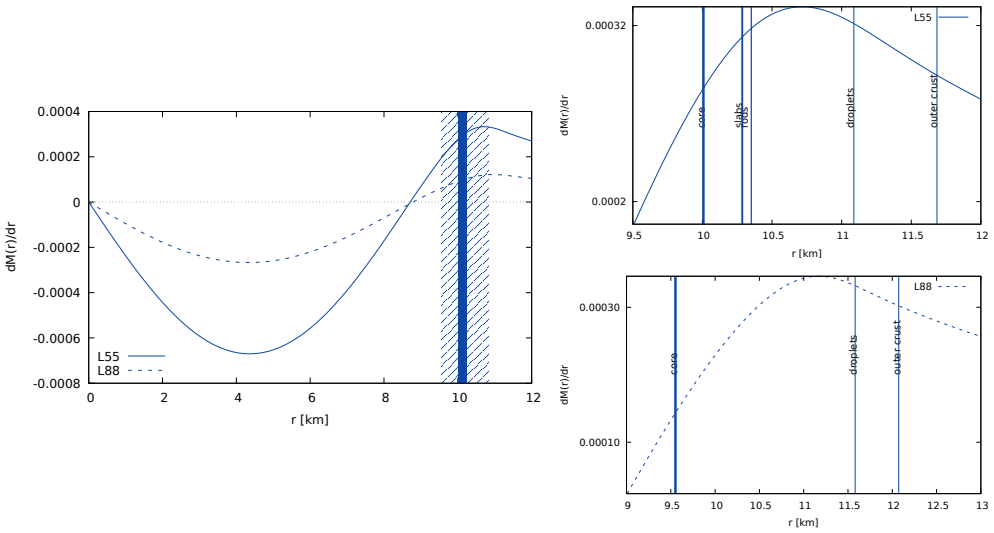

Figure 5.14: Derivative of the magnetic potential, as function of the radial coordinate for a $M_b = 1.5\mathrm{M}_\odot$ star with $B_S = 4.4 \times 10^{16}$ G. Full lines correspond to the model with $L = 55$ MeV, whilst dashed lines come from the $L = 88$ MeV model. In the plots on the right we have amplified the region inside the crust and identified the location of the transition between the different pasta phases.

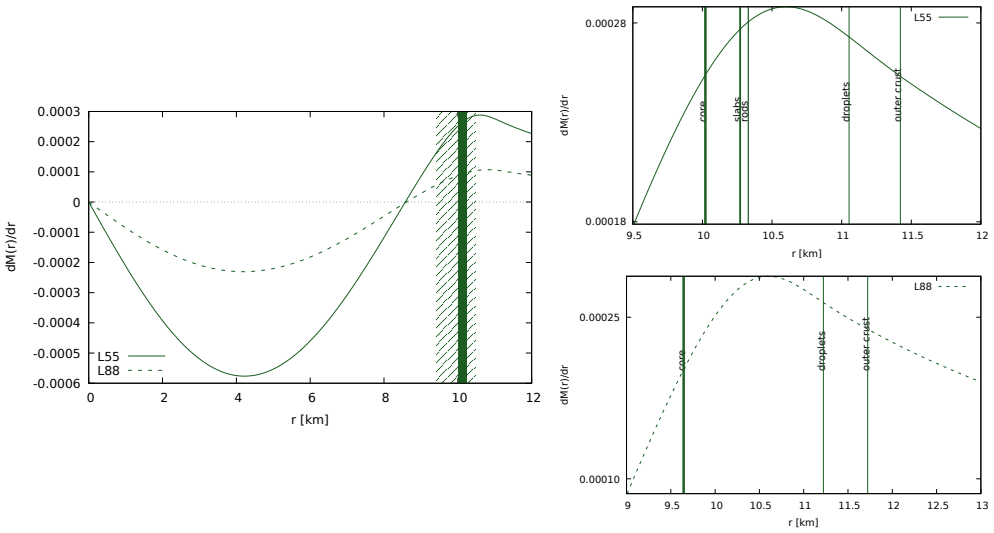

Figure 5.15: Derivative of the magnetic potential, as function of the radial coordinate for a $M_b = 1.8\mathrm{M}_\odot$ star with $B_S = 4.4 \times 10^{16}$ G. Full lines correspond to the model with $L = 55$ MeV, whilst dashed lines come from the $L = 88$ MeV model. In the plots on the right we have amplified the region inside the crust and identified the location of the transition between the different pasta phases.

5.2.1 Inclusion of rotation

The study of the effects of both rotation and magnetic fields on the microscopical properties of the star and, as well, on its geometry are not new and they trace back to the work by [34]. Here, we are interested on evaluating these effects on the inner crust of the star. We begin by showing, in Figure 5.16, how the crust size is altered by the inclusion of magnetic field. We compare, using the same masses and models as before, the deformation of a star with a surface field of $B_S = 2.6 \times 10^{16}$G in two different scenarios:

- without rotation – for each case we chose the CFA that gives a field of 2.6×10^{16}G at the surface;
- with rotation – we chose the right combination of both the frequency and CFA that resulted in a star with $B_S = 2.6 \times 10^{16}$ G. These pairs of results can be found in Table 5.4

Table 5.4: frequency, f, and CFA used in the calculations of magnetized rotating stars.

L (MeV)	M_b ($M_\odot$)	f (Hz)	CFA
55	1.2	548.055913471	7293.37264983
55	1.5	594.038994537	5690.64096289
55	1.8	639.312646658	4658.81936968
88	1.2	520.739975764	7658.41016529
88	1.5	575.814541748	5943.18027505
88	1.8	625.044983051	4843.77960609

Such approach was necessary because if we fix the CFA value or, equivalently, the magnetic moment, the magnetic field measured inside the star will vary as we increase the rotation frequency. This phenomenon can be seen in Figure 5.17.

Turning our attention back to Figure 5.16, we see that, even though in both scenarios the stars possess the same magnetic field value, the rotating stars are much more deformed.

We followed the same strategy used in Figure 5.16 in order to analyze the effects of rotation on the magnetic potential. These results are shown in Figure 5.18. We wanted in particular to see, as we did in the non-rotating case, where the minimum of the potential would be located in respect to the crust. Surprisingly we found out that when we include rotation the convex shape of the magnetic function disappears and, thus, there is no local minimum.

It is important to note that in both cases shown in Figure 5.18 the stars have the same surface magnetic field, but they were calculated with different CFA values (for the same reasons discussed before). Therefore, one could wonder whether the differences shown in Figure 5.16 are not simply because of the fact that we are considering different CFA values. In order to eliminate this possibility, in Figure 5.19 we used the same current function amplitude [2] (the ones shown in Table 5.4) and, as before, the non-rotating case presents the convex shape, with its very noticeable minimum.

As we said before, in the rotating case we chose a combination of both CFA and frequency values that would originate a star with a field of 2.6×10^{16}G at its surface. The frequencies that verified that condition were in the range of 548 – 626 Hz. We observed that for lower frequencies the magnetic potential function still possess a minimum. Therefore, there exists a *critical frequency* at which the magnetic potential minimum disappears and the Lorenz force points always in the same direction throughout the star. It would be interesting to understand whether this effects is relevant for the description of extreme phenomena in the crust of the star, and how this critical frequency might depend on the EOS.

[2] In the previous case, the CFA values used in the non-rotating case were such that $B_S = 2.6 \cdot 10^{16}$ G, and were obtained by interpolating a B_S VS CFA curve.

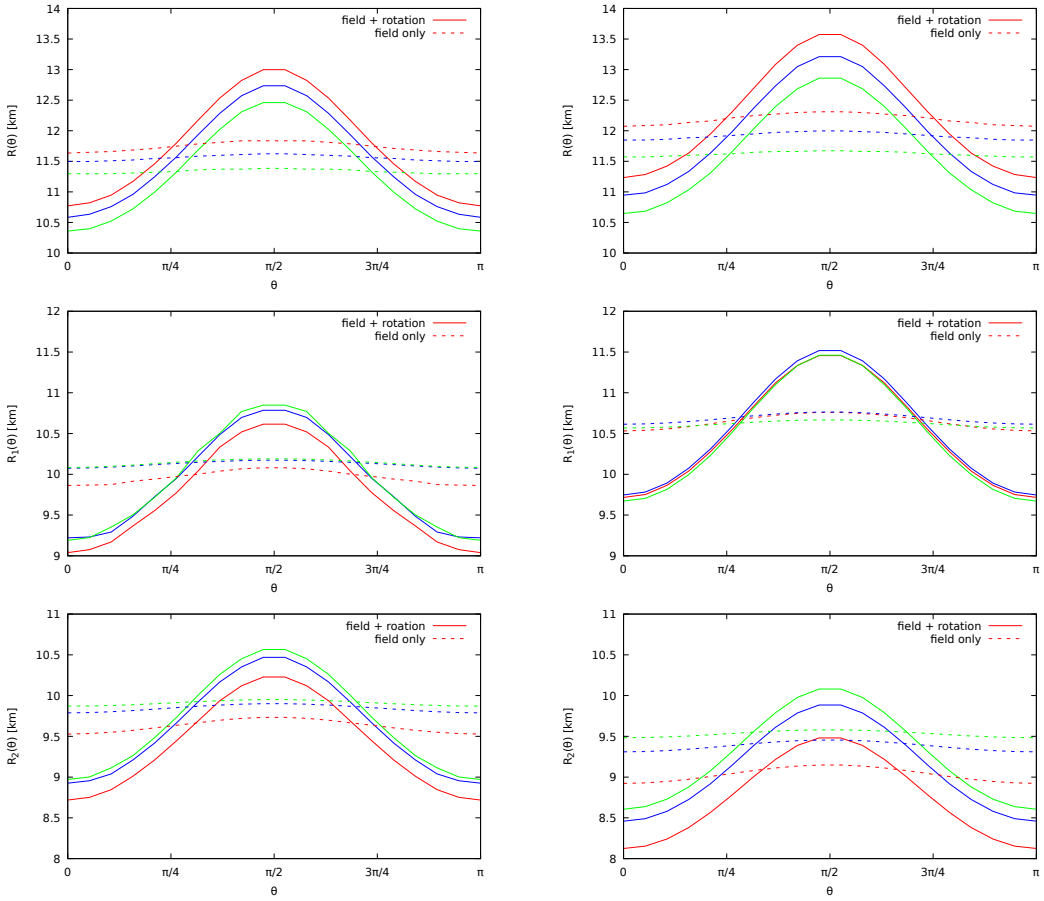

(a) $L = 55$ MeV (b) $L = 88$ MeV

Figure 5.16: Comparison between the effects of both magnetic fields and rotation with those of magnetic field only. In both cases the surface field is 2.6×10^{16} G. On the left panel we have results with $L = 55$ MeV and on the right $L = 88$ MeV.

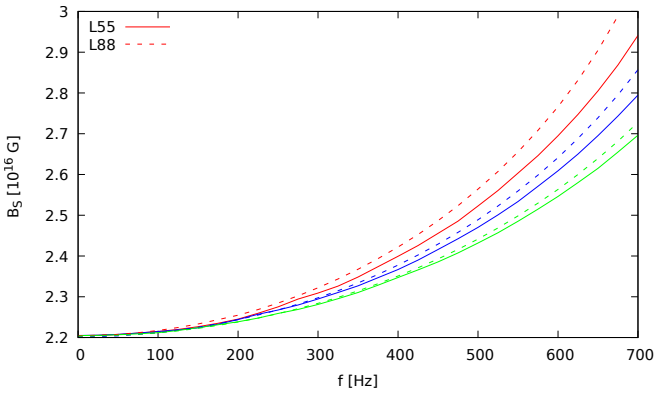

Figure 5.17: Radial component of the magnetic field at the surface pole, B_S, as function of rotation frequency, f. Full lines correspond to the model with $L = 55$ MeV, whilst dashed lines come from $L = 88$ MeV. The colours red, blue and green correspond to baryon masses $1.2M_\odot$,$1.5M_\odot$ and $1.8M_\odot$, respectively.

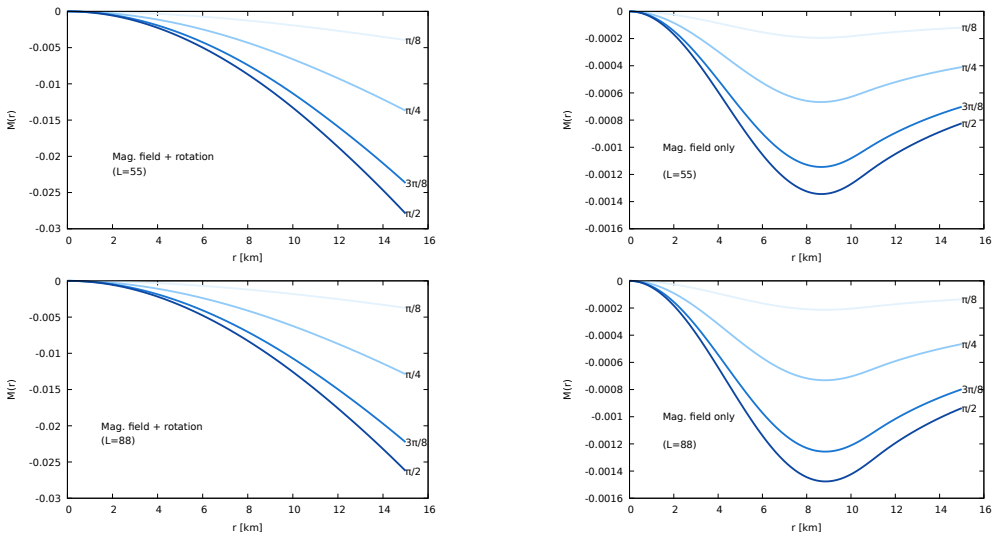

(a) with rotation (b) without rotation

Figure 5.18: Magnetic potential for magnetized rotating stars (panels on the left) and stars without rotation (on the right), setting $M_b = 1.5M_\odot$. As before, in both cases magnetic field at the surface is 2.6×10^{16} G. The rotation frequencies are those presented in Table 5.4.

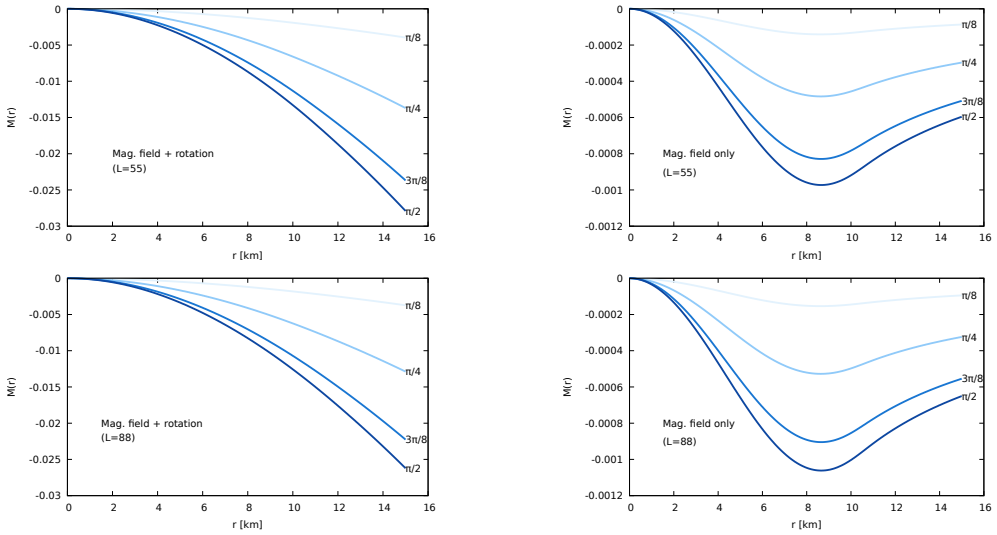

(a) with rotation (b) without rotation

Figure 5.19: Magnetic potential for magnetized rotating stars (panels on the left) and stars without rotation (on the right),setting $M_b = 1.5\mathrm{M}_\odot$. Here the current function amplitude is fixed for each model (we used the values presented in Table 5.4).

Chapter 6

Conclusion

In this thesis we studied the effects of strong magnetic fields and rotation on the properties of the neutron star crust. We have taken into account the intermediate zone at the crust-core transition that were introduced in [2], which consists in a region where stable and unstable matter interchange. We have studied stars of three different baryon masses: 1.2, 1.5 and 1.8 $M_{\odot}$. The neutron star matter was described using two different parameterizations of the NL3$\omega\rho$ model: $L = 55$ and $L = 88$ MeV.

As expected, we verified that the lightest stars become more deformed in the presence of magnetic fields. We also verified that the model with $L = 88$ MeV is more sensible to the presence of magnetic fields, which might be because of its greater proton fraction.

The total size of the crust is model dependent, which is consequence of the fact that the densities from which the crust-core transition is defined depend on the proton fraction which, in turn, is directly related to the symmetry energy slope, L [41]. We verified that both the total crust and the extended region have smaller values for the model with $L = 88$ MeV.

Our most interesting results come from the study of the magnetic potential function, M, whose gradient is proportional to the Lorenz force. In [35] it was verified that the Lorenz force changes sign inside the neutron star. Here we verified that for both models and for the three masses considered, the points at which this change of sign occur are always located in the core. In other hand we verified that, when we exclude the effects

of rotation, the Lorenz force possess two local maximums: one of them falls into the core and the other is located in the crust, which might be linked with the breaking of matter in the region. For the $L = 55$ MeV model this maximum falls in the zone populated by droplets. Although, this maximum is also near the rod like configurations, which are easier to deform. In our study of the pasta phases we have only considered M evaluated at the equatorial plane. It would be interesting to see if, for other directions, the maximum is located in other pasta phases.

Finally, we verified that the minimum of the magnetic potential, and thus the change of sign point, vanishes for rotating frequencies higher than a certain critical value. When this frequency is reached, the Lorenz force no longer posses a local minimum. It would be interesting to understand whether this effect is relevant for the description of extreme phenomena in the crust of the star, and how this critical frequency might depend on the EOS.

Bibliography

[1] P. Haensel, A.Y. Potekhin, and D.G. Yakovlev. *Neutron Stars 1: Equation of State and Structure (Astrophysics and Space Science Library) (v. 1)*. Springer, 2006.

[2] Jianjun Fang, Helena Pais, Sagar Pratapsi, Sidney Avancini, Jing Li, and Constança Providência. Effect of strong magnetic fields on the crust-core transition and inner crust of neutron stars. *Physical Review C*, 95(4), April 2017.

[3] Sushan Konar. Magnetic fields of neutron stars. *Journal of Astrophysics and Astronomy*, 38(3), September 2017.

[4] F. Cipolletta, C. Cherubini, S. Filippi, J. A. Rueda, and R. Ruffini. Fast rotating neutron stars with realistic nuclear matter equation of state. *Physical Review D*, 92(2), July 2015.

[5] D. G. Ravenhall, C. J. Pethick, and J. R. Wilson. Structure of matter below nuclear saturation density. *Physical Review Letters*, 50(26):2066–2069, June 1983.

[6] et al Eric Gourgoulhon. Lorene. `https://lorene.obspm.fr/`, 1999.

[7] Gordon Baym, Christopher Pethick, and Peter Sutherland. The ground state of matter at high densities: Equation of state and stellar models. *The Astrophysical Journal*, 170:299, December 1971.

[8] Norman K. Glendenning. *Compact Stars: Nuclear Physics, Particle Physics, and General Relativity (Astronomy and Astrophysics Library)*. Springer, 2000.

[9] G. A. Lalazissis, J. König, and P. Ring. New parametrization for the lagrangian density of relativistic mean field theory. *Physical Review C*, 55(1):540–543, January 1997.

[10] M. Dutra, O. Lourenço, S. S. Avancini, B. V. Carlson, A. Delfino, D. P. Menezes, C. Providência, S. Typel, and J. R. Stone. Relativistic mean-field hadronic models under nuclear matter constraints. *Physical Review C*, 90(5), November 2014.

[11] Tuhin Malik, N. Alam, M. Fortin, C. Providência, B. K. Agrawal, T. K. Jha, Bharat Kumar, and S. K. Patra. GW170817: Constraining the nuclear matter equation of state from the neutron star tidal deformability. *Physical Review C*, 98(3), September 2018.

[12] J. Boguta and A.R. Bodmer. Relativistic calculation of nuclear matter and the nuclear surface. *Nuclear Physics A*, 292(3):413–428, December 1977.

[13] C. J. Horowitz and J. Piekarewicz. Neutron radii of 208pb and neutron stars. *Physical Review C*, 64(6), November 2001.

[14] Constança Providência. Relativistic Hadronic Matter And Phase Transition. *International Journal of Modern Physics E*, 16(09):2680–2719, October 2007.

[15] Helena Pais and Constança Providência. Vlasov formalism for extended relativistic mean field models: The crust-core transition and the stellar matter equation of state. *Physical Review C*, 94(1), July 2016.

[16] A Rabhi, C Providência, and J Da Providência. Stellar matter with a strong magnetic field within density-dependent relativistic models. *Journal of Physics G: Nuclear and Particle Physics*, 35(12):125201, October 2008.

[17] A. Broderick, M. Prakash, and J. M. Lattimer. The equation of state of neutron star matter in strong magnetic fields. *The Astrophysical Journal*, 537(1):351–367, July 2000.

[18] M. Nielsen, C. Providncia, and J. da Providncia. Collective modes in relativistic nuclear matter: Classical approach. *Physical Review C*, 44(1):209–217, July 1991.

[19] Eitan Tadmor. A review of numerical methods for nonlinear partial differential equations. *Bulletin of the American Mathematical Society*, 49(4):507–554, 2012.

[20] Bernard Schutz. *A First Course in General Relativity.* Cambridge University Press, 2009.

[21] Eric Gourgoulhon. An introduction to the theory of rotating relativistic stars, 2010.

[22] Jeffrey Winicour. Characteristic evolution and matching. *Living Reviews in Relativity*, 15(1), January 2012.

[23] Jörg Frauendiener. Conformal infinity. *Living Reviews in Relativity*, 3(1), August 2000.

[24] Frans Pretorius. Numerical relativity using a generalized harmonic decomposition. *Classical and Quantum Gravity*, 22(2):425–451, January 2005.

[25] Lee Lindblom, Mark A Scheel, Lawrence E Kidder, Robert Owen, and Oliver Rinne. A new generalized harmonic evolution system. *Classical and Quantum Gravity*, 23(16):S447–S462, July 2006.

[26] Eric Gourgoulhon. *3+1 Formalism in General Relativity.* Springer Berlin Heidelberg, 2012.

[27] Charles W. Misner, Kip S. Thorne, and John Archibald Wheeler. *Gravitation.* Princeton University Press, 2017.

[28] Sean Carroll. *Spacetime and Geometry: An Introduction to General Relativity.* Pearson, 2003.

[29] Carles Bona, Carlos Palenzuela-Luque, and Carles Bona-Casas. *Elements of Numerical Relativity and Relativistic Hydrodynamics.* Springer Berlin Heidelberg, 2009.

[30] John Baez and Javier P Muniain. *Gauge Fields, Knots and Gravity.* WORLD SCIENTIFIC, October 1994.

[31] Silvano Bonazzola, Eric Gourgoulhon, Philippe Grandclément, and Jérôme Novak. Constrained scheme for the einstein equations based on the dirac gauge and spherical coordinates. *Physical Review D*, 70(10), November 2004.

[32] S. Bonazzola, E. Gourgoulhon, M. Salgado, and J. Mark. Axisymmetric rotating relativistic bodies: A new numerical approach for 'exact' solutions. *Astronomy and Astrophysics*, 278(2), 1993.

[33] Nikolaos Stergioulas. Rotating stars in relativity. *Living Reviews in Relativity*, 6(1), June 2003.

[34] S.; Gourgoulhon E.; Novak J. Bocquet, M.; Bonazzola. Rotating neutron star models with a magnetic field. *Astron. Astrophys.*, 301(757), 1995.

[35] B. Franzon, R. Negreiros, and S. Schramm. Magnetic field effects on the crust structure of neutron stars. *Physical Review D*, 96(12), December 2017.

[36] M. Bocquet, S. Bonazzola, E. Gourgoulhon, and J. Novak. Rotating neutron star models with magnetic field. 1995.

[37] Richard Arnowitt, Stanley Deser, and Charles W. Misner. Republication of: The dynamics of general relativity. *General Relativity and Gravitation*, 40(9):1997–2027, August 2008.

[38] ivoabs. Lorene pythontools, August 2019.

[39] R. O. Gomes, H. Pais, V. Dexheimer, C. Providência, and S. Schramm. Limiting magnetic field for minimal deformation of a magnetized neutron star. *Astronomy & Astrophysics*, 627:A61, July 2019.

[40] Isaac Vidaña, Constança Providência, Artur Polls, and Arnau Rios. Density dependence of the nuclear symmetry energy: A microscopic perspective. *Physical Review C*, 80(4), October 2009.

[41] C. Ducoin, C. Providência, A. M. Santos, L. Brito, and Ph. Chomaz. Cluster formation in compact stars: Relativistic versus skyrme nuclear models. *Physical Review C*, 78(5), November 2008.